Resolving the origins of secretory products and anthelmintic responses in a human parasitic nematode at single-cell resolution.

Clair R. Henthorn[1], Paul M. Airs[1], Emma K. Neumann[2], Mostafa Zamanian[1*]

[1] Department of Pathobiological Sciences, University of Wisconsin-Madison, Madison, WI USA

[2] Pathology and Laboratory Medicine, School of Medicine and Public Health, University of Wisconsin-Madison, Madison, WI USA

[*] mzamanian@wisc.edu

Abstract

Nematode excretory-secretory (ES) products are essential for the establishment and maintenance of infections in mammals and are valued as therapeutic and diagnostic targets. While parasite effector proteins contribute to host immune evasion and anthelmintics have been shown to modulate secretory behaviors, little is known about the cellular origins of ES products or the tissue distributions of drug targets. We leveraged single-cell approaches in the human parasite *Brugia malayi* to generate an annotated cell expression atlas of microfilariae. We show that prominent antigens are transcriptionally derived from both secretory and non-secretory cell and tissue types, and anthelmintic targets display distinct expression patterns across neuronal, muscular, and other cell types. While the major classes of anthelmintics do not affect the viability of isolated cells at pharmacological concentrations, we observe cell-specific transcriptional shifts in response to ivermectin. Finally, we introduce a microfilariae cell culture model to enable future functional studies of parasitic nematode cells. We expect these methods to be readily adaptable to other parasitic nematode species and stages.

23 # Introduction

24 Lymphatic filariasis (LF) is a chronic and debilitating neglected tropical disease caused by the
25 filarial nematodes *Wuchereria bancrofti, Brugia malayi,* and *Brugia timori.* Infective-stage larvae
26 are transmitted by mosquitoes to the human definitive host, where they develop and molt to
27 adult stages that persist in the lymphatics and produce blood-circulating pre-larval stage
28 microfilariae (mf) (Roberts et al., 2009). LF afflicts an estimated 51 million individuals in tropical
29 and subtropical climates around the world and endangers nearly a billion individuals worldwide
30 (Local Burden of Disease 2019 Neglected Tropical Diseases Collaborators, 2020; World Health
31 Organization, 2018). Chronic cases of LF manifest in elephantiasis, an extreme buildup of
32 lymph resulting in stigmatizing disfiguration and additional socioeconomic challenges (Ton et
33 al., 2015; Weiss, 2008). Mass drug administration (MDA) in endemic settings with
34 combinations of ivermectin (IVM), diethylcarbamazine (DEC), and albendazole (ABZ) is used to
35 disrupt parasite transmission, but this approach is only effective with years of repeated
36 treatment. Additionally, contraindications for antifilarial drugs exist in regions co-endemic for
37 other filarial parasites (Chippaux et al., 1996). With no cure and the growing threat of
38 resistance to anthelmintics (Campbell, 1982; Geary et al., 2011, 2010a; Ismail et al., 1999;
39 Osei-Atweneboana et al., 2011; Wolstenholme et al., 2015), there is a clear need to improve
40 our understanding of basic biological processes that underpin the host-parasite interaction.
41
42 The excretory-secretory (ES) products of parasitic nematodes are known to be essential for
43 parasite survival within the host (Harnett, 2014; Hotterbeekx et al., 2021; Lightowlers and
44 Rickard, 1988). Despite the general understanding that the ES system is a conduit for the
45 release of immunomodulatory proteins and extracellular vesicles that promote parasite survival,
46 the biology of the ES system has yet to be investigated in medically important parasitic
47 nematodes. Profiling of secretions (Bennuru et al., 2011; Harischandra et al., 2018; Hewitson

et al., 2008; Kaushal et al., 1982; Moreno and Geary, 2008; Zamanian et al., 2015) across the filarial nematode life cycle has helped identify antigens that have been pursued therapeutically and diagnostically (Harnett, 2014; Kalyanasundaram et al., 2020; Maizels et al., 2001; Morris et al., 2013), but the origins of these proteins and the tissue systems that underlie their release at the host-parasite interface are unknown. Recent studies have also implicated secretory processes as a target of existing anthelmintics (Moreno et al., 2021, 2010). Ivermectin causes rapid clearance of mf from host blood at concentrations that do not cause overt fitness effects on cultured parasites (Geary et al., 2010b). This disconnect is reconciled by a model whereby IVM unmasks mf from the host immune system by inhibiting protein and vesicle secretion (Rao et al., 1987; Vatta et al., 2014; Zahner et al., 1997). While the ES apparatus is thought to be the primary source of immunogenic proteins in the mf stage, the cells that comprise this structure and control secretion have not been characterized.

Clear morphological descriptions of the filarial ES system are currently restricted to the mf stage, but microscopy studies confirm that this structure is present in L3 and adult parasites (Airs et al., 2022; Landmann et al., 2010; Mutafchiev et al., 2014; Tongu, 1974). Filarial parasites possess tubular ES systems featuring a single large excretory cell connected through a cytoplasmic bridge to an excretory vesicle and pore (Tongu, 1974). In the free-living model nematode *Caenorhabditis elegans*, the ES system is a well-studied and critical osmoregulatory and excretory organ made up of a pore cell, duct cell, excretory/canal cell, and canal-associated neurons (CAN) (Sundaram and Buechner, 2016). However, significant diversification of ES anatomy and function between *C. elegans* and filariae and more generally across nematode clades (A. F. Bird, 1991) demands more species-specific approaches to the study of excretory-secretory systems.

73 Single-cell transcriptomics has facilitated resolution of cellular processes and functions that are
74 masked in tissue level or bulk transcriptomic approaches. Single-cell suspensions generated
75 from tissue dispersions of free-living nematodes (Zhang et al., 2011) have enabled high
76 dimensional transcriptomic analysis of cell types across developmental stages (Ben-David et
77 al., 2020; Cao et al., 2017; Packer et al., 2019; Taylor et al., 2021; Zhang et al., 2011) and
78 provide a pathway to the characterization of essential cells and tissues in related parasites,
79 including those that control secretory behaviors. However, viable cell suspensions have yet to
80 be leveraged to transcriptomically profile human, animal, or plant parasitic nematodes at
81 single-cell resolution. This goal is complicated in many species by life cycle patterns that can
82 limit tissue availability and anatomical variation that can affect access to rare cell types.
83
84 Here, we applied single-cell approaches to generate and annotate a cell atlas of gene
85 expression in *B. malayi* microfilariae and to map secretory-associated cell types and the
86 distributions of prominent antigens and anthelmintic targets. We evaluated the effects of
87 anthelmintics on parasite cells and the amenability of mf cell suspensions to longer-term
88 culture. These data and methods allowed for novel inferences about the origins of
89 immunogenic molecules, the mechanism of action of existing anthelmintics, and provide an
90 avenue for future functional studies of *B. malayi* cell populations. We expect that many of these
91 tools can be extended to other medically important parasitic nematodes.

Results

Generation of viable single-cell suspensions from *Brugia malayi* microfilariae

We focused our efforts on generating single-cell suspensions from the blood-circulating microfilariae (mf) stage of the human parasitic nematode *B. malayi*. This pre-larval life stage is small (~177-230 µm in length, ~5-7 µm in diameter) but can be isolated from peritoneal fluid of infected jirds in large quantities (millions), potentially facilitating insight into early parasite development and the capture of rare cell types. Using larval tissue dispersion protocols from *C. elegans* as a scaffold, we developed a single-cell dissociation protocol in *B. malayi* mf that accounts for the unique biology of this parasite stage (**Figure 1A**). Microfilariae suspensions recovered from the jird peritoneal cavity are developmentally asynchronous and include an abundance of host cells, tissue debris, embryos, and nonviable mf, all of which contribute to transcriptomic contamination. To reduce contamination and enrich for viable mf, peritoneal lavages were filtered using Sephadex PD-10 desalting columns (Galal et al., 1989; Rathaur et al., 1987). This method reliably recovered high yields (60-70%) of highly motile mf which were then used as input into tissue dispersion reactions (**Figure 1B**).

B. malayi mf are encapsulated within an impermeable eggshell of carbohydrates including chitin (Fuhrman and Piessens, 1985). We treated filtered mf with chitinase to penetrate this sheath and allow downstream dispersion reagents to access the underlying cuticle and worm body. Chitinase treatment did not cause complete exsheathment, but produced a visible shrinking effect in the tail and head spaces indicating sheath breach (**Figure 1C**). SDS-DTT treatment was optimized to weaken protective structures (sheath and cuticle) of chitinase-treated worms while preserving cell health. Incubation in diluted SDS-DTT effectively

compromised cuticular structure and inhibited motility without causing parasite death (**Figure 1-figure supplement 1**). Recoverable inhibition of motility, as revealed by subsequent wash steps, served as visual confirmation of the efficient weakening of the cuticle and preservation of the underlying body.

The generation of single-cell suspensions was completed using pronase enzymatic digestion and mechanical disruption by continuous pipetting. Progression of the pronase digestion was monitored throughout the treatment (**Figure 1D)**. mf cuticles were visibly compromised after approximately 20 min of digestion, where the midsection of the filarial body plan exhibits protrusions that break and release cells. Progression of the reaction yields a mixed suspension of worm segments, single-cells, and intact mf, and an abundance of single-cells can be seen by 30 min. Continuous mechanical disruption was essential to encourage the breakage of worms and release of single-cells. The majority of undigested worms were removed by centrifugation and filtration resulting in a highly viable single-cell mf suspension for downstream applications.

High content imaging of cell suspensions confirms capture of rare parasite cell types

The integrity of cells retrieved from *Brugia* mf dispersions was assessed by imaging flow cytometry. A total of 20,000 objects were assessed and 15,683 were identified as debris, undigested worm segments, or nonviable cells as indicated by negative Calcein-AM staining, a cell-permeable viability dye that remains within healthy cells after acetoxymethyl (AM) cleavage by non-specific esterase activity. The remaining 4,317 objects were analyzed using post-acquisition image features to identify 2,893 objects as live, single cells that displayed round cellular and nuclear morphology (**Figure 1E**). While the majority of recovered cells have a

140 diameter of 5.23 ± 0.77 μm, each mf is known to possess a large and morphologically distinct
141 secretory cell that is critical to parasite survival and immune evasion in the host (Tongu 1974;
142 Hewitson et al. 2009). The *Brugia* secretory cell is hypothesized to be responsible for the
143 release of prominent antigens, extracellular vesicles, and nucleic acids that operate at the host-
144 parasite interface. Classical descriptions of the mf ES system highlight the secretory cell as a
145 large cell with bipolar canal extensions (Moreno et al., 2010; Nelson and Riddle, 1984;
146 Sundaram and Buechner, 2016). We mined cells in our dataset that match this description and
147 identified a total of 11 cells with bipolar appendages that are notably the largest identifiable
148 cells (8.46 ± 0.77 μm in diameter) in this life stage (**Figure 1E**). Each mf possesses a single
149 secretory cell among hundreds of total cells and this recovery rate (0.4%) falls within the
150 expected range, providing us confidence that our dispersion protocol captures both common
151 and rare cell types.

152 Single-cell transcriptomic atlas identifies conserved and unique pre-larval 153 cell populations

154 To define the transcriptional profiles of *B. malayi* microfilariae cell types, we generated a single-
155 cell RNA-seq (scRNA-seq) library from cell suspensions. Dimensional reduction of 46,621
156 filtered cells via Uniform Manifold Approximation and Projection (UMAP) (McInnes et al., 2018)
157 identified 27 transcriptionally distinct clusters. Across all cells in the dataset, a median of 230
158 genes and 267 reads per cell were achieved (**Figure 2-figure supplement 1**). Transcript
159 abundance of single-cells strongly correlated with microfilariae bulk gene expression (Reaves
160 et al., 2018) (**Figure 2A inset**, $r = 0.85$, $R^2 = 0.72$, $p = 2.2 \times 10^{-16}$), providing additional
161 evidence that our single-cell pipeline largely recapitulates the cell type distribution and
162 transcriptional profile of the intact parasite. An analysis of *B. malayi* transcription factors shows
163 both specific and broad-based transcription factor activity that aligns with known *C. elegans*

164 patterns (**Figure 2-figure supplement 2**). For example, *lin-14* exhibits broad expression in the
165 *B. malayi* mf scRNA-seq data and is congruent with broad expression of the transcription factor
166 in *C. elegans* (Taylor et al., 2021). In contrast, *C. elegans* has multiple cell type restricted
167 transcription factors including ciliated sensory neuron transcription factor *Cel-daf-19* and body
168 wall muscle specific transcription factors *Cel-hlh-1* and *Cel-unc-120* (Taylor et al., 2021), both
169 of which show restricted cluster expression in the *B. malayi* mf scRNA-seq atlas. These
170 analyses provide confidence in the biological signal acquired through scRNA-seq. Markers for
171 well-characterized *C. elegans* cell types (**Figure 2-figure supplement 3**) with one-to-one *B.*
172 *malayi* orthologs were used to annotate 16 UMAP clusters (**Figure 2A**) and pseudobulk
173 analysis confirms the robustness of these markers for differentiating cell types (**Figure 2-figure**
174 **supplement 4**). In total 18,317 cells (39.3% of global count) were assigned a cell type
175 annotation. Among these, 6,223 cells were identified as muscle derived (13.3% of global count)
176 and 5,527 cells expressed pan-neuronal markers (11.9% of global count). Additional
177 identifiable clusters include those representing canal-associated cells, coelomocytes,
178 mesodermal tissues, and a pre-alimentary canal related cell type.
179
180 Cell types belonging to the mesoderm lineage include 10,284 cells (22% of global count). Body
181 wall muscle cells represent the majority of the mesodermal cells identified (clusters 2 and 19)
182 and are distinctly categorized based on expression of *Bma-hlh-1* (Krause et al., 1994) and
183 markers shown to be enriched in *B. malayi* body wall muscle such as actin and multiple
184 myosins (*Bma-myo-3*, *Bma-unc-54.1*, *Bma-unc-54.2*, *Bma-act-1*) (Morris et al., 2015). An
185 additional two clusters (clusters 9 and 17) strongly express markers associated with
186 mesodermal lineage *C. elegans* cell types (enteric and vulval), including *Cel-hlh-8, Cel-hlh-2*,
187 and *Cel-mls-1* orthologs (Packer et al., 2019; Philogene et al., 2012). Differentially expressed
188 genes between the two clusters are proteins of unknown function and could not be further
189 parsed. Also belonging to the mesodermal cell lineage in *C. elegans* are coelomocytes,

190 phagocytic scavengers located within the pseudocoel. Using coelomocyte-specific *C. elegans*
191 orthologs (*Bma-cup-4*, *Bm6921*, *Bma-unc-122*, *Bma-let-381*), cluster 6 was annotated as
192 coelomocytes. These data show that mesodermal cells in the post-embryonic and pre-larval mf
193 state include well differentiated body wall musculature and coelomocytes and underdeveloped
194 enteric and vulval muscle structures.
195
196 Pan-neuronal *C. elegans* markers (*sbt-1, ric-4, ida-1, egl-3, egl-21*) were used to identify nine
197 clusters of putative neurons expressing all five markers (303 genes and 358 reads per cell)
198 (**Figure 2B**). We were able to further resolve a cluster of motor neurons (cluster 11) and
199 interneurons (cluster 23) characterized by one-to-one orthologs of the *C. elegans* motor neuron
200 marker (*Cel-unc-4*) and DVA tail interneuron marker (*Cel-nlp-12*), respectively (**Figure 2-figure**
201 **supplement 4**). Clusters 13 and 27 express *Bma-daf-19*, an ortholog of the RFX-family
202 transcription factor *Cel-daf-19* shown to be directly responsible for cilia development in ciliated
203 sensory neurons as well as genes involved in ciliogenesis (**Figure 2-figure supplement 3**)
204 (Blacque et al., 2005; Chen et al., 2006; Narasimhan et al., 2015; Swoboda et al., 2000).
205 These two clusters have been annotated as ciliated sensory neurons. Known genes involved in
206 neurotransmitter synthesis and transport were used to map neuropeptidergic (cluster 26) and
207 aminergic neurons (clusters 24 and 25) (**Figure 2B**). Acetylcholine is the primary excitatory
208 nematode neurotransmitter and we used cholinergic pathway genes (*Bma-cha-1*, *Bma-cho-1*,
209 and *Bma-ace-2*) to locate cholinergic neurons. The motor and interneuron neuronal clusters
210 (11 and 23) express *Bma-cha-1* and *Bma-cho-1* in 10-15% of all captured cells. Clusters 3-5
211 exhibit more abundant expression of *Bma-cha-1* (**Figure 2-figure supplement 5**) but no other
212 neuronal markers, cholinergic or pan-neuronal, and may represent a cholinergic neuronal
213 developmental state.
214

215 The phylogenetic distance between free-living clade V *C. elegans* and filarial clade III
216 nematodes is associated with known differences in anatomy (Chitwood and Chitwood, 1950)
217 and localization of some orthologous proteins (Moreno et al., 2010), which limits efforts to
218 comprehensively map all cell types across species (**Figure 2-figure supplement 6**). Cell types
219 and structures unique to filarial nematodes demand different annotation approaches. A cluster
220 of 503 cells (cluster 22) uniquely displays high expression of chitinases (*Bma-cht-1.1*, *Bma-cht-*
221 *1.2*, *Bma-cht-1.3*) and the immunomodulatory vaccine candidates *Bma-val-1* and *Bm97.*
222 Chitinase has been shown to be stored in the inner body of microfilariae which is positioned
223 between the excretory and G1 cells and is hypothesized to act as the precursor for the
224 intestinal tract of the developing larvae in the mosquito (McLaren, 1972; Wu et al., 2008). The
225 combination of chitinase and molting proteins within this segregated cluster support the
226 annotation of cluster 22 as inner body-associated cells.

227 Among *C. elegans* excretory-secretory cell types, only canal-associated (CAN) cell-specific
228 markers could be associated with a *B. malayi* single-cell cluster. *B. malayi* orthologs (*Bma-pks-*
229 *1*, *Bma-acbp-6*, *Bma-ceh-10*) of CAN markers identify cluster 14 as ES canal-associated cells
230 (1,006 total cells). Given the unique cell composition and structural adaptations of the ES
231 system in filarial nematodes, identification of additional secretory cell types demands other
232 approaches.

233 Identification of secretory-related cell types using FACS and RNA-seq
234 approaches

235 We exploited the large size of the *B. malayi* secretory cell as a means to enrich for and profile
236 this rare cell type within single-cell suspensions. The largest viable cells within a *B. malayi*
237 microfilariae suspension were FAC-sorted and pooled for downstream RNA-seq (**Figure 3A**
238 and **Figure 3-figure supplement 1**). The transcriptional profiles of these outlier cells were

239 compared to smaller round cells that typify the mf cell population, and unique identifiers of the
240 largest cells were mapped to the single-cell atlas UMAP. Cluster 15 shows a clear overall
241 enrichment for the 78 genes more highly expressed in this sorted cell population (**Figure 3B**
242 and **Figure 3-source data 1**) and individual cells within this putative secretory cell cluster
243 represent the largest group coexpressing different subsets of these markers (**Figure 3C** and
244 **Figure 3-source data 2**).
245
246 To assess whether the *C. elegans* excretory cell would have provided information relevant to
247 unearthing the filarial secretory cell, we carried out pooled single-cell RNA-seq of GFP tagged
248 (*vha-1p::*GFP) and sorted *C. elegans* excretory cells (**Figure 3D, Figure 3-source data 3,** and
249 **Figure 3-figure supplement 2**). Established and new *C. elegans* excretory cell markers
250 identified through this effort lack clear orthologs or display no meaningful overlap with highly or
251 uniquely expressed orthologous markers found in the *B. malayi* secretory cell. This aligns with
252 the distinct evolutionary history of the ES system in filariae and the parasite-specific functions
253 the secretory cell is likely to perform in the host context.

254 Abundantly-secreted parasite proteins have diverse tissue origins

255 We next investigated the origins of prominent molecules known to be secreted by blood-
256 circulating mf and that are likely necessary for parasite immune evasion and survival. Studies
257 have identified secreted proteins and antigens across the intra-mammalian life cycle stages
258 (Bennuru et al., 2011; Harischandra et al., 2018; Hewitson et al., 2008; Kaushal et al., 1982;
259 Moreno and Geary, 2008; Zamanian et al., 2015). We mined the literature for a comprehensive
260 list of major antigens, vaccine targets, diagnostic markers, and other notable secreted proteins
261 and probed the scRNA-seq data to identify their transcriptional origins (**Figure 3E** and **Figure**
262 **3-source data 4**). Transcripts encoding for secreted proteins exhibit variable patterns of
263 expression across the body and very few are specifically localized to the secretory cell (cluster

264 15). Some prominent antigens that are expressed across many tissue types (*Bma-tpi-1* and
265 *Bma-cpi-2*) have been localized to the ES apparatus via whole-mount antibody staining
266 (Moreno et al., 2010), an observation that is likely reconciled by aggregation and secretion of
267 these proteins through the ES apparatus. Additional broadly expressed antigens that are
268 included as vaccine targets and diagnostic markers include *Bma-tpi-1*, *Bma-sxp-2,* and
269 *Bm3837* (**Figure 3E** and **Figure 3-figure supplement 3**) (Krushna et al., 2009; Lalitha et al.,
270 2002; Morris et al., 2013).
271
272 We identified prominent antigens and diagnostic markers that exhibit much more tissue-
273 restricted expression in both secretory and non-secretory cell types. *Bma-val-1*, *Bm97*, and
274 chitinases (*Bma-cht-1.1* and *Bma-cht-1.2*) have strong and nearly undivided expression in the
275 inner body (**Figure 3-figure supplement 3**). Muscle and undefined cell types also harbor an
276 abundance of interesting transcripts (ex. *Bma-unc-15*, *Bma-sxp-1*, *Bm7564*). Notable genes
277 that showed strong or exclusive expression in the annotated secretory cells include
278 microfilariae-specific serpin *Bma-srp-2* and diagnostic antigens *Bm10631* (*BmR1)* (Greene et
279 al., 2022) and *Bm14*, a Cys_2His_2 zinc finger (C2H2-ZF) transcription factor (**Figure 3E**).

280 C2H2-ZF transcription factors are enriched in annotated secretory cells

281 We sought to further characterize transcripts that are specifically enriched in the annotated
282 secretory cell. A greater fraction of proteins with transcripts enriched in the secretory cell
283 contain signal peptides (43%) compared to other cell types (**Figure 4A** and **Figure 4-source**
284 **data 1**). Signal peptides may not be required for release into the host environment as many
285 proteins identified in ES studies do not possess this targeting signal (Hewitson et al. 2008).
286 41.8% of proteins with transcripts enriched in the secretory cell are predicted to contain
287 transmembrane domains (**Figure 4B** and **Figure 4-source data 2**). Subpopulations of these
288 putative membrane-spanning proteins may potentially serve as candidate hidden antigens that

289 may evade recognition by the host immune system but may be highly accessible to vaccine-
290 induced antibodies (Munn 1997).
291
292 We investigated the distribution of C2H2-ZF transcription factors in light of the high abundance
293 and restriction of the diagnostic marker *Bm14* in the secretory cell cluster. We generated a
294 phylogeny of *B. malayi* C2H2-ZF transcription factors and identified two expanded subgroups
295 that are secretory cell specific and that lack one-to-one *C. elegans* orthologs (**Figure 4C**).
296 Several of these transcription factors were also detected in the bulk RNA-seq data of FAC-
297 sorted "largest" cells. The C2H2-ZF family is a large, diverse family of proteins (Kang and Kim,
298 2000; Razin et al., 2012). Previous studies have reported an enrichment of this transcription
299 factor class in mf-derived ES products and elevated expression of these genes in mf (Bennuru
300 et al., 2011; Choi et al., 2011). The role of these proteins in ES cell types is poorly understood,
301 but may involve governing gene regulatory events at the host-parasite interface or to help
302 adapt mf for the stark environmental transition from the mammalian host to the mosquito
303 vector.

304 Mapping anthelmintic targets across the microfilarial body

305 Modulation of ES processes may explain the mechanism of action of essential anthelmintics
306 (Moreno et al., 2021) and a deeper understanding of the cellular or physiological processes
307 that regulate ES systems may identify new therapeutic strategies. Ion channels and structural
308 proteins in the neuromuscular system are the primary targets of nearly all anthelmintics. To
309 identify the distribution of the known and putative targets of existing and emerging
310 anthelmintics within the microfilarial body, we mapped the cell type locations of β-tubulins, cys-
311 loop ligand gated ion channels (LGICs), and additional ionotropic receptors (**Figure 5A**).
312 Benzimidazoles compromise nematode cell structural integrity by acting as microtubule
313 inhibitors, but the specific β-tubulin target(s) are unknown in filariae despite the use of ABZ in

314 MDA programs. The four β-tubulin *B. malayi* proteins exhibit broad expression across the mf
315 body, with *Bma-btub-1* (*Bm4733*) most highly expressed compared to all other β-tubulins
316 (**Figure 5A** and **5B**). This β-tubulin also has the highest sequence similarity to the benzimidazole
317 target in *C. elegans* (*ben-1*), and we hypothesize that *Bma-btub-1* is responsible for mediating the
318 antifilarial action of ABZ. *Bma-tbb-4* and *Bma-mec-7* were minimally represented but found in
319 muscle and neuronal cell types. The coexpression of β-tubulins in *C. elegans* cells provides
320 redundancy that allows for normal growth in *Cel-ben-1* loss-of-function mutants (Driscoll et al.
321 1989). Single-cell coexpression of β-tubulins within individual *B. malayi* mf cells shows strong
322 association between *Bma-tbb-4* and *Bma-btub-1* and a moderate association between *Bma-*
323 *btub-1* and *Bma-btub-2* (**Figure 5C**), pointing to potential redundancy and compensatory drug
324 response mechanisms.
325
326 Transient receptor potential (TRP) channels are gaining recognition as anthelmintic targets
327 (Park et al., 2019) and the TRPC-like channel *Bma-trp-2* has recently been implicated as a
328 target of DEC (Verma et al., 2020; Williams et al., 2022). We observed the expression of all 10
329 *B. malayi* TRP channels with at least one TRP channel subunit expressed in every cell type
330 (**Figure 5A** and **Figure 5-figure supplement 1**). *Bma-trp-2* facilitates inward calcium currents
331 upon activation and results in subsequent opening of the SLO-1 K^+ channel (Verma et al.,
332 2020; Williams et al., 2022), the proposed target of the macrofilaricidal emodepside (Kashyap
333 et al., 2019). The majority of *Bma-trp-2* and *Bma-slo-1* transcripts are found in body wall
334 muscle (clusters 2 and 19), consistent with electrophysiological assays (Kashyap et al., 2019;
335 Verma et al., 2020) and the paralytic effect of emodepside.
336
337 The glutamate-gated chloride channels (GluCls) are of special interest as the targets of the
338 macrocyclic lactones and as regulators of ES processes. There is strong evidence that IVM
339 acts on muscle-expressed GluCls adjacent to the secretory apparatus leading to suppression

340 of secretory cargo and host clearance of mf (Harischandra et al., 2018; Li et al., 2014; Loghry
341 et al., 2020; Moreno et al., 2010). The *B. malayi* GluCl complement (*Bma-avr-14, Bma-glc-2,*
342 *Bma-glc-3,* and *Bma-glc-4*) display expression in neuronal and muscle cell types (**Figure 5A**
343 and **5B**). *Bma-avr-14* is noted as an important subunit for IVM sensitivity (Dent et al., 2000),
344 and the expression of *avr-14* in annotated muscle cell types is consistent with its expression in
345 muscle surrounding the ES pore (Moreno et al., 2010). While functional *B. malayi* GluCl
346 channels have been constituted in heterologous systems to determine IVM sensitivity
347 (Choudhary et al., 2022; Lamassiaude et al., 2022), not all subunit compositions are amenable
348 to expression and it is unclear what channel formations best reflect the native state
349 (Lamassiaude et al., 2022). To improve predictions of native channel compositions, we
350 examined the correlation of GluCl subunit expression in individual cells and identified *Bma-avr-*
351 *14* and *Bma-glc-4* as the most commonly coexpressed GluCl subunits (**Figure 5C**). *Bma-avr-*
352 *14* was also coexpressed with *Bma-glc-2*, a combination reported to be IVM-sensitive, however
353 *Bma-glc-2* was minimally expressed and was not coexpressed with any other GluCl subunit.
354
355 Nicotinic acetylcholine receptors (nAChR) are activated by levamisole and other cholinergic
356 anthelmintics. As expected, the subunits that comprise *L*-type and *P*-type nAChR channels are
357 mainly restricted to the body wall muscle (**Figure 5A** and **Figure 5-figure supplement 1**).
358 Single-cell coexpression analysis of nAChRs reveals that *Bma-acr-15* could be an essential
359 and missing component of our understanding of nAChR composition and function in filarial
360 nematodes (**Figure 5C**). These data enrich our understanding of tissue-specific targeting of the
361 major anthelmintic classes and provide new cell-specific leads belonging to traditionally
362 druggable receptor families.

363 ## Measuring the effects of anthelmintics on the viability and transcriptional
364 states of isolated cells

365 With a view of how anthelmintic targets are distributed across cells and tissues, we set out to
366 investigate anthelmintic responses at single-cell resolution. To first validate flow cytometry as a
367 cell viability quantification approach, single-cell suspensions from the same *B. malayi*
368 dispersion reaction were exposed to DMSO, methanol (nonviable), or remained untreated
369 (viable). Cell viability was successfully measured using DRAQ5 (nucleated objects) and
370 Calcein Violet-AM, a shorter wavelength version of the Calcein-AM dye(**Figure 6A**). We also
371 confirmed that cell health did not decline significantly after dissociation and incubation on ice in
372 media for up to 8 hr and that DMSO at concentrations required for drug solubility did not
373 compromise cell health (**Figure 6B**).

374 Next we examined the effects of three major anthelmintic classes (macrocyclic lactones,
375 benzimidazoles, and nicotinic agonists) on parasite cell viability. Homogenous cell preparations
376 from independent parasite infection cohorts were split into parallel treatment conditions and
377 cells were exposed to drugs for a 20 min incubation period prior to flow cytometry analysis.
378 Dose response curves (50 nM, 1 μM, 50 μM, 100 μM) were completed using IVM, levamisole
379 (LEV), and albendazole sulfoxide (AZS), the active metabolite of albendazole (**Figure 6C**). We
380 did not observe a significant decrease in cell viability in any of the primary classes of drug at
381 pharmacologically relevant concentrations, however, higher concentrations of IVM did produce
382 a cytotoxic effect (EC_{50} = 51 ± 5.16 μM) (**Figure 6D**).

383 While these anthelmintics did not exhibit strong cell-cidal activity, we reasoned they may
384 differentially alter gene expression in various cell types. Single-cell RNA-sequencing was
385 carried out using a homogenous *B. malayi* mf cell suspension that was equally split with one
386 half receiving short-term IVM exposure at a concentration that does not affect cell viability (1

387 μM for 20 min). Compared to the untreated control, muscle, neurons, and unannotated cell
388 types revealed the most significant and abundant upregulation of genes in response to IVM
389 exposure (**Figure 6E** and **Figure 6-source data 1**). The greatest transcriptional shift occurs in
390 muscle cells, which house the highest transcriptional abundance of GluCls (**Figure 5-figure**
391 **supplement 1**). Differentially expressed genes of interest include serine protease inhibitor
392 *Bma-srp-2*, a highly abundant ES product released from mf, which showed the greatest
393 increase in expression in unannotated cluster 8 ($Log_2FC > 2.8$) but was also significantly
394 upregulated in 9 of 27 clusters. The IVM response was additionally characterized by
395 upregulation of genes previously identified in bulk RNA-seq studies (*Bm10661, Bm228,*
396 *Bm9776, Bma-srp-2, Bm8514, Bma-unc-54.2, Bm33, Bm13260, Bma-rps-28*) (Ballesteros et
397 al., 2016) and proteins with unassigned functions.

398 Cell culture of dispersed mf suspensions provides avenue for single-cell
399 functional analyses

400 Historically, cell culture models have revolutionized biological understanding and progress
401 towards drug discovery and development in mammalian systems. The complex
402 cyclodevelopmental life cycle of filarial worms and the absence of immortalized cell lines
403 derived from any helminth species complicate the translation of these approaches to
404 helminthology. While dispersions of embryonic *Brugia* cells have been performed, the captured
405 cells do not differentiate in culture (Higazi et al., 2004), limiting the advantages of the system.
406 To enable future studies of cell biology and drug interaction at single-cell resolution, we sought
407 to establish a filarial nematode cell culture system for the longer-term maintenance of adherent
408 and differentiated cell populations. To this end, *B. malayi* mf primary cell cultures were plated
409 onto peanut-lectin coated chamber slides and imaged to assess cell adherence and health.
410 Highly viable populations of adhered cells were observed after a 24 hr incubation in 10% FBS

411 L-15 media (**Figure 7A**). We next plated primary cells onto peanut-lectin coated surfaces in
412 microtiter plate format to monitor viability over a longer time frame using high-throughput
413 imaging. Adhered cells remained viable at 96 hr as indicated by Calcein-AM fluorescence
414 (**Figure 7B** and **Figure 7-figure supplement 1**). We assessed the mitotic activity of these cells
415 using an EdU proliferation assay and determined these cells are not actively dividing in the
416 current culture conditions (**Figure 7-figure supplement 2**). Further development and
417 adaptation of this method will support transgenic manipulation and functional studies of
418 differentiated *B. malayi* cell populations.

419 Discussion

420 Excretory-secretory products released by parasitic nematodes into the host environment are
421 recognized as key molecular mediators for the establishment and maintenance of infections.
422 The secretory processes that underlie host immune evasion and modulation may serve as
423 targets for existing (Loghry et al., 2020; Moreno et al., 2010) and future drugs. Despite this, our
424 superficial knowledge of the structure and function of the secretory apparatus of human
425 parasitic nematodes has limited our understanding of the molecular events that drive host-
426 parasite interactions. To help address these knowledge gaps, we introduce the first single-cell
427 transcriptomic atlas of a parasitic nematode and leverage this resource to resolve tissue and
428 cell-specific gene expression patterns that allow for inferences about the origins of secretory
429 products and antiparasitic mechanisms of action.
430
431 We developed a single-cell dissociation and RNA-seq protocol to generate a transcriptomic
432 atlas of the blood-circulating microfilariae stage of the human filarial parasite *B. malayi*. Using
433 marker genes specific for terminal and developing cell types, we annotated ~30% of the cells
434 represented in our dataset as muscle and neuronally derived. Ten clusters in the dataset

435 (61.5% of total cell count) remain unannotated. The use of a pre-larval developmental stage
436 containing cells that have yet to terminally differentiate and a developmentally asynchronous
437 mf population likely contributed to difficulties in comprehensive disentanglement and
438 annotation of transcriptionally distinct cell clusters. The potential to annotate cells is further
439 confounded by the unknown biological functions of genes that distinguish different clusters.
440 Many unannotated clusters in the dataset may be resolved by deeper single-cell profiling and
441 validation efforts. For instance, cluster 7 lowly expresses several *C. elegans* genes found in
442 sensory neurons related to cilium assembly and organization (*osm-1, dyf-11, ccep-290, ift-74,*
443 *dyf-17, che-3, T12B3.1*) (Peter N. Inglis, Guangshuo Ou, Michel R. Leroux, and Jonathan M.
444 Scholey, 2006) but lowly expresses only a subset of pan-neuronal markers (**Figure 2-figure**
445 **supplement 3**).
446
447 Knowledge from *C. elegans* was useful in identifying rare cell populations such as
448 coelomocytes or canal-associated cells, but alternative approaches were necessary for the
449 identification of clade-diverged secretory cells. Pooled RNA-seq of sorted cell populations
450 enriched for the morphological characteristics of the *B. malayi* secretory cell allowed for the
451 annotation of secretory-like cells within the mf cell atlas. Surprisingly, prominent secreted
452 proteins and antigens show different patterns of transcript distribution across cell populations,
453 establishing that immunomodulatory ES products originate from different parasite tissues. For
454 example, the diagnostic marker *BmR1* (*Bm10631*) is exclusively transcribed in the secretory
455 cell while the vaccine immunogens *Bma-val-1* and *Bm97* are restricted to the inner body. It is
456 possible that many of the proteins encoded by these transcripts share a common exit route
457 from the worm through the ES apparatus (Moreno et al., 2010) or that many of these proteins
458 are exposed to the host by dead or dying parasites. The later possibility may warrant greater
459 focus on targets that are actively transcribed in the secretory cell of viable parasites.
460

461 The inner body is a chitinase-enriched (*Bma-cht-1.1, Bma-cht-1.2*) intestinal tract precursor,
462 and its breakdown leads to the release of chitinase and exsheathment within the mosquito (Wu
463 et al., 2008). Exposure of mf to IVM prevents later exsheathment in the mosquito (U. R. Rao,
464 A. C. Vickery, B. H. Kwa, J. K. Nayar, 1992), which we speculate is consistent with suppression
465 of ES function leading to the trapping of inner-body enzymes. This view of the mf ES apparatus
466 as a secretory choke point in the parasite life cycle offers a control target relevant to both the
467 arthropod and mammalian hosts. Later developmental stages in the parasite life cycle (L3 and
468 adults) present additional orifices and interfaces for host interaction, necessitating other
469 approaches to parse out the relationship between ES products and the ES apparatus in these
470 stages.
471
472 The putative targets for mainstay anthelmintics are known, but their tissue distributions
473 throughout the filarial worm body are unresolved. Further, the native subunit compositions of
474 the ion channel drug targets of the macrocyclic lactones and nicotinic agonists are unknown.
475 We leveraged these data to map the expression of known and putative antifilarial drug targets
476 across cell types and to predict ion channel subunit associations from single-cell coexpression
477 analysis. These predictions can guide the reconstitution and functional expression of
478 pharmacologically relevant ion channels in heterologous studies of channel function and
479 anthelmintic responses. We directly assessed the effects of anthelmintics on the viability of
480 isolated cells, showing that the major anthelmintic classes do not elicit cell death at
481 pharmacologically relevant concentrations. This suggests that the primary action of these drugs
482 requires cell-cell connectivity. The action of IVM in *C. elegans* is innexin-dependent (Dent et
483 al., 2000), underscoring the importance of gap junctions in the signaling cascade that results in
484 the whole-organism drug effect. To capture early transcriptional events that drive IVM action in
485 the mf stage, we identified core genes that are upregulated across isolated cell types in
486 response to acute drug exposure. Future studies that compare the transcriptional trajectories of

487 cells exposed to drug before and after dissociation may help resolve the role of cell-cell
488 communication and various compensatory responses in anthelmintic mechanisms of action.

489 Finally, we developed a protocol for culturing cells derived from *B. malayi* microfilariae tissue
490 dispersions. Efforts that improve our ability to manipulate these dispersed cell populations have
491 the potential to expand our understanding of parasite cell biology and receptor-mediated
492 responses to external drug and chemical stimuli. While there has been great progress in the
493 genetic manipulation of filariae (Higazi et al., 2002; Liu et al., 2020, 2018; Xu et al., 2011),
494 germline transgenesis has proven difficult and optimized protocols cannot overcome a two-host
495 life cycle with a long parasite pre-patent period. Transfection of cultured *Brugia* mf primary cells
496 with promoter-driven constructs and CRISPR reagents can help circumnavigate some existing
497 limitations and facilitate the study of parasite protein function. Although primary cells are often
498 difficult to transfect or transduce, optimization of both viral and non-viral approaches has
499 helped overcome these challenges in a cell-type specific manner (Chong et al. 2021).
500 Collectively, the continued development of these resources and associated methods can help
501 answer outstanding questions about the nematode parasite-host-drug interface.

502 Materials and Methods

503 Data and Code Availability

504 All data and scripts used for data analysis and visualization are publicly available at
505 https://github.com/zamanianlab/Bmsinglecell-ms and in a Zenodo repository
506 (https://zenodo.org/record/7110316). Single-cell and FACS-pooled RNA-seq data has been
507 deposited into NIH BioProjects PRJNA874113 and PRJNA874749. The processed data can
508 also be explored at https://github.com/zamanianlab/BmSC_shiny as a locally run RStudio
509 Shiny application.

510 ## Parasite and *C. elegans* Strains

511 *Brugia* microfilariae (mf) were supplied by the NIH/NIAID Filariasis Research Reagent
512 Resource Center (FR3) (Michalski et al., 2011). *B. malayi* mf were used for all experiments
513 except for the imaging flow cytometry data where the anatomically equivalent *B. pahangi*
514 species was used due to parasite availability at the time of the assay. Mf extracted from the jird
515 peritoneal cavity were filtered and cultured in RPMI-1640 with L-glutamine (Sigma-Aldrich, St.
516 Louis, MO) supplemented with 10% fetal bovine serum (FBS) (Thermo Fisher, Waltham, MA)
517 and 50 µg/mL penicillin/streptomycin (P/S) (Thermo Fisher, Waltham, MA). All experiments
518 used mf incubated at 37°C+5% CO_2 for at least 1 hr prior to experimentation within 24 hours of
519 host extraction, or stored at 4°C overnight in fresh media and processed within 48 hours of
520 host extraction. *C. elegans* strain BK36 was acquired from the *Caenorhabditis* Genetics Center
521 (CGC). *C. elegans* strains N2 and BK36 were maintained at 20ºC on NGM plates seeded with
522 *Escherichia coli* OP50. Worms were propagated by routine picking of L4 stage worms to
523 seeded NGM plates.

524 ## Microfilariae Purification

525 *Brugia* mf were purified using a PD-10 desalting column (Cytiva, Marlborough, MA) to remove
526 host cells, debris, embryos, and perished microfilariae as previously described (Galal et al.,
527 1989) with minor changes. Briefly, the PD-10 column was equilibrated by passing 25 mL of
528 RPMI-1640 with L-glutamine through the column. Mf were centrifuged at 2,000 rpm for 10 min
529 and the supernatant was drawn off leaving 5 mL of peritoneal fluid and the mf pellet. Mf were
530 resuspended and the entirety of the suspension was transferred to the equilibrated PD-10
531 column. RPMI-1640 medium was added to the column in 5 mL increments, and the flowthrough
532 was checked every 5 mL for the presence of mf and host peritoneal cells. Mf were collected
533 when no host peritoneal cells were present in the flowthrough and until mf were no longer

534 being eluted. Recovered mf were washed twice in RPMI-1640 by centrifugation, resuspended
535 in RPMI-1640, and allowed to recover at 37°C for at least one hour prior to beginning a single-
536 cell dissociation.

537 Microfilariae Single-cell Dissociation

538 PD-10 column purified mf from the same jird parasite infection cohort were used as input for
539 *Brugia* dispersions at ~1 million mf per reaction. The mf were aliquoted to a 1.5 mL
540 microcentrifuge tube, pelleted, and resuspended in 2 mg/mL chitinase from *Streptomyces*
541 *griseus* (Sigma-Aldrich, St. Louis, MO) and incubated at 37ºC with light agitation for 20 min. mf
542 were washed once with 1 mL RPMI-1640 medium and the chitinase-treated pellet was
543 resuspended in SDS-DTT (200 mM DTT, 0.25% SDS, 20 mM HEPES, pH 8.0, 3% sucrose)
544 diluted 1:4 in Leibovitz's L-15 medium without phenol red (Gibco, Waltham, MA) and an
545 adjusted osmolality of 340 mOsm using 1 M sucrose. 200 µL of diluted SDS-DTT was added to
546 the mf pellet and placed on a nutator for 6 min, where the mf are alive but not thrashing. 1 mL
547 of L-15 medium was added to the tube and centrifuged at 16,000 rcf for 30 sec at 4ºC. The
548 supernatant was removed and the pellet was resuspended in 1 mL fresh L-15 medium. The mf
549 were washed a total of 5 times or until the smell of SDS-DTT was no longer lingering. The
550 pellet was resuspended in 100 µL pronase from *Streptomyces griseus* (VWR, Radnor, PA) at a
551 concentration of 15 mg/mL in L-15 medium (340 mOsm). The reaction was continuously
552 pipetted 100 times every 5 minutes either manually or by the use of the Repetitive Pipettor
553 robot. The reaction was monitored by eye by checking small aliquots throughout the digestion.
554 The reaction was stopped with ice cold 1 mL L-15+10% FBS when most mf were broken open
555 and single-cells were clearly visible in the background (~30 min). The dispersed cells and
556 remaining worms and debris was pelleted by centrifugation at 1,000 rcf for 6 min at 4ºC. The
557 pellet was resuspended in 1 mL cold L-15+10% FBS and centrifuged briefly for 5 sec at 1,000
558 rcf to separate remaining large debris and single-cells. The top ~900 µL of cell suspension was

559 drawn up into a 1 mL syringe and pushed through a reusable syringe filter (Millipore,
560 Burlington, MA) containing 7 μm mesh (Component Supply, Sparta, TN). The filtrates were
561 combined and used in downstream applications. A standard hemocytometer was the most cost
562 and time effective cell count estimation method with the caveat that differentiating cell versus
563 debris was very difficult. Comparisons between the methods can be found in the supplemental
564 material (**Figure 1-source data 1**).

565 Imaging Flow Cytometry

566 Single-cell suspensions maintained on ice were incubated with DRAQ5 (500 nM) (Biolegend,
567 San Diego, CA) and Calcein-AM (500 nM) (Biolegend, San Diego, CA) in L-15+10% FBS for a
568 minimum of 20 min on ice prior to acquisition. An Amnis ImageStream Mark II Imaging Flow
569 Cytometer equipped with a 60X objective and a 2-laser (488 nm and 642 nm), 6-channel
570 detection system was used for single-cell imaging acquisition. Samples were gated based on
571 viability (DRAQ5+, Calcein-AM+). Analysis of images was completed using the Amnis Image
572 Data Exploration and Analysis Software (IDEAS) and the integrated Feature Finder Wizard to
573 distinguish viable single-cells from the population based on a subset of hand-picked single-
574 cells as a training dataset.

575 Anthelmintic Drug Dose Responses

576 Single-cell suspensions generated from *B. malayi* microfilariae were subjected to drug
577 treatment using ivermectin (IVM) (Fisher), albendazole sulfoxide (AZS) (Fisher Scientific,
578 Hampton, NH), and levamisole (LEV) (VWR, Radnor, PA). Biological replicates were taken
579 from separate jird parasite infection cohorts. Drugs were suspended in DMSO (Santa Cruz
580 Biotechnology, Dallas, TX) and added to cell suspensions at 50 nM, 1 μM, 50 μM, and 100 μM
581 for 20 min on ice with a final DMSO concentration of 0.1%. At the completion of incubation, the

582 cell suspensions were centrifuged at 1,000 rcf for 6 min and as much supernatant as possible
583 was removed without disrupting the pellet. Cells were resuspended in 300 µL of L-15+10%
584 FBS containing DRAQ5 (2.5 µM) and Calcein Violet-AM (0.75 µM) and stored on ice until flow
585 cytometry analysis. Treatment controls included untreated and DMSO only (0.1%) treated cell
586 suspensions. Controls for spectral flow cytometry included L-15+10% FBS, unstained cells,
587 and DRAQ5 (2.5 µM) and Calcein Violet-AM (0.75 µM) fluorescence minus one controls.
588 Additional controls of L-15+100 µM IVM and unstained cells+100 µM IVM were necessary to
589 confirm the presence of IVM precipitation at high concentrations picked up by the spectral flow
590 cytometer. Viability curves of single-cell suspensions over time were generated using cells from
591 a *B. malayi* mf dissociation reaction (input of ~1 million mf) and split to create three treatment
592 groups (untreated, 0.1% DMSO, and methanol fixed) with four samples each to cover four
593 timepoints over 8 hr. Samples were stained with DRAQ5 and Calcein Violet-AM 30 min prior to
594 analysis on the flow cytometer. Methanol fixed cell suspensions served as a cell death control
595 and were prepared by adding 300 µL methanol (chilled to -20ºC) to 100 µL cell suspension and
596 incubated at 4ºC for 30 min prior to staining and analysis. Samples were analyzed on a Cytek
597 Aurora Spectral Cytometer equipped with five lasers (355 nm UV, 405 nm Violet, 488 nm Blue,
598 561 nm Yellow-Green, and 640 nm Red). The laser light channels include a forward scatter
599 and side scatter off of both the blue and violet lasers and has 64 fluorescence channel
600 detectors. Selection of single-cell entities was completed using FSC-A vs FSC-H followed by
601 selection of cells that are DRAQ5(+) and Calcein Violet-AM(+). Gated cells with a Calcein
602 Violet-AM intensity greater than 105 were considered Calcein Violet-AM(+) and viable. Percent
603 viability was calculated by dividing the Calcein Violet-AM(+) population by the total DRAQ5(+)
604 population and the EC_{50} was calculated using the R statistical software with the drc package
605 (Ritz et al., 2015).

606 ## 10x Genomics Preparation and Sequencing

607 A *B. malayi* mf single-cell suspension was split into two equal parts and one part was treated
608 with 1 μM IVM in DMSO (1.0% final v/v) for 20 min on ice. At the end of incubation, the cells
609 were centrifuged at 1,000 rcf for 6 min at 4ºC, the supernatant was removed, and the cells
610 were resuspended in L-15+10% FBS. Cells were normalized to 1,400 cells/μL as estimated by
611 standard hemocytometer (INCYTO, Cheonan-si, South Korea) to target an input of 12,000 cells
612 for capture on the 10x Genomics Chromium controller. A single technical and biological
613 replicate was completed for each treatment. The 10x Genomics 3' Single Cell RNA-seq
614 protocol (v3.1 NextGEM User Guide Rev.D) was followed to generate the gel bead-in-
615 emulsions (GEMs) and post cDNA amplification cleanup. The cDNA library was prepared using
616 the Chromium Dual Index TT primers and the Single Cell 3' v3.1 Reagents and user guide. The
617 library was sequenced on an Illumina NovaSeq6000 to generate ~550 M reads across control
618 and drug-treated samples (2x50 bp on S1 flow cell).

619 ## scRNA-seq Mapping

620 The ivermectin treated and untreated *B. malayi* mf scRNA-seq data were mapped and
621 processed independently. Single-cell RNA-seq data were mapped to the *Brugia malayi*
622 reference genome (Wormbase, WS285) using 10x Genomics Cell Ranger 5.0.1 analysis
623 pipeline. The 10x Genomics 3' Single Cell RNA-seq protocol is strongly biased towards the 3'
624 regions of mRNA which are not well annotated in *B. malayi* thus requiring a modified reference
625 genome to improve the mapping rates of the scRNA-seq data. The 3' UTRs were artificially
626 extended by 50, 100, 150, 200, 250, 300, 400, and 500 bp as previously described with
627 modifications (Taylor et al., 2021). Briefly, the scRNA-seq data was mapped using the Cell
628 Ranger pipeline for each iteration and the total reads for each gene in every iteration were
629 summarized across all of the cells. The gene counts for each extension were normalized to the

630 gene count of the 500 bp extension and the optimal extension length for each gene was
631 determined by identifying the extension that provided at least a 90% increase in mapping rate.
632 The *B. malayi* scRNA-seq raw data was mapped one final time using the newly generated
633 reference genome containing the optimal 3' UTR extension length for each gene. The Cell
634 Ranger filtered output drastically underreported the estimated cell count and is not optimized
635 for small, low expressing cells. Therefore the raw Cell Ranger output was used for filtration and
636 preprocessing.

637 scRNA-seq Bioinformatics Analysis

638 The raw Cell Ranger barcode matrix output for each scRNA-seq dataset (untreated and +IVM
639 treated) was filtered to remove empty droplets using the cluster-based R package scCB2 (Ni et
640 al., 2020). Using EmptyDrops (ED) as a scaffold, scCB2 increases the power to distinguish real
641 cells from background empty droplets as well as low-expressing, small cells by pooling low-
642 count barcodes with similar gene expression patterns. The cluster is then compared against
643 the estimated background population to identify irrelevant barcodes. This method of empty
644 droplet filtration allows for the identification of small, low-expressing cells which are prevalent in
645 the *B. malayi* mf single-cell dispersions. To facilitate this testing, scCB2's CB2FindCell()
646 function was used and droplets with 100 or fewer total counts were used to estimate the
647 background distribution (lower = 100). A False Discovery Rate (FDR) was set to 0.01. The
648 resulting cell matrix was converted to a Seurat object and genes detected in less than 3 cells
649 were omitted. The filtered cell population was then used as input into the R package SoupX
650 (Young and Behjati, 2020) to estimate the contribution of cell free mRNA contamination
651 captured in each droplet. Because SoupX can provide a better estimate of contamination when
652 cluster information is supplied, the scCB2-filtered datasets were taken through the Seurat
653 pipeline (Hao et al., 2021) to identify clusters. Briefly, each dataset was log normalized and
654 variable features were selected using the "vst" method and 2,000 features. PCA analysis was

655 completed using 50 dimensions, which were used for clustering and dimension reduction via
656 UMAP. The raw and clustered datasets were used as input to SoupX with cells containing 0-25
657 total UMI counts used to estimate the “soup”. A lower UMI count to estimate the “soup” was
658 used to avoid unintentionally including lower expressing neuronal cells. The estimated
659 contamination fraction for the untreated and treated datasets were calculated to be
660 approximately 0.13 and 0.10 respectively, and the count matrix was adjusted accordingly using
661 the adjustCounts() function. The ambient mRNA contamination was removed and additional
662 filters were applied on the remaining cell population. Cells with high mitochondrial
663 representation (greater than or equal to 10% of all UMIs per cell) were identified using the
664 mitochondrial markers *Bm5157, Bma-nduo-4,* and *Bma-ctc-1 (Qing et al., 2021)*. Cells were
665 removed from the population if a single gene represented greater than or equal to 15% of the
666 total cell transcripts, had greater than 2,500 total genes expressed, and more than 1,800 total
667 UMIs. These cutoffs were determined by the distributions and to omit potential doublets. The
668 remaining count matrices for the untreated and treated datasets contained > 10,000 genes with
669 21,131 and 25,490 cells respectively. Seurat 4.1.1 was used for downstream integration and
670 normalization. First, each matrix was log normalized and the top 2,000 variable genes were
671 identified using the FindVariableFeatures() functions using the “vst” selection method. Variable
672 genes were then used to integrate the control and treated datasets using the
673 FindIntegrationAnchors() and IntegrateData() functions with default parameters. Principal
674 component analysis (dims = 50) for dimension reduction was completed for clustering and
675 visualization of the combined datasets. Differentially expressed genes between clusters was
676 completed using the FindConservedMarkers() function in Seurat, which uses a Wilcoxon Rank
677 Sum test and Bonferroni p-value correction to account for false positives. Genes with an
678 adjusted p-value > 0.05 were considered significant. Differentially expressed genes in
679 response to IVM treatment were identified using Seurat’s FindMarkers() function with a
680 logfc.threshold = 0.25. Treated and untreated cells were compared by cluster assignment.

681 ## Pseudobulk Analysis

682 Pseudobulk analysis was completed using the single-cell dataset generated from *B. malayi* mf.
683 The raw read counts from the gene-by-cell expression matrix were aggregated for each cluster
684 and treatment assignment. Each cluster and treatment combination was handled as an
685 individual sample (1_tBM = 1 sample). The size of the aggregated read counts for each sample
686 was TMM normalized using edgeR (v3.38.4) (Robinson et al. 2010). Genes with less than 10
687 aggregated read counts across all samples were removed from the dataset. The pseudobulk
688 gene expression matrix was $\log_2(x+1)$ and the resulting counts were median-centered. Genes
689 and samples were hierarchically clustered in R using the ClassDiscovery package (v3.4.0)
690 (Coombes 2021) using an uncentered Pearson correlation to calculate the distance matrix and
691 complete-linkage for clustering. The gene expression heatmap was generated using pheatmap
692 (v1.0.12) (Kolde 2018) where color indicates the level of expression (yellow=upregulated;
693 blue=downregulated).

694 ## Phylogenetic Analyses

695 *B. malayi* transcription factors were identified using a reciprocal blastp and HMM approach
696 using *C. elegans* transcription factors obtained from the CIS-BP database (v.2.0) (Weirauch et
697 al. 2014) as input. Only transcription factors that were supported by direct experimental
698 evidence were considered. Multiple sequence alignment was completed using MAFFT (v.7)
699 with an iterative refinement approach (E-INS-i) and poorly aligned regions were removed using
700 trimAl (v.1.2) (Capella-Gutiérrez et al. 2009). A maximum likelihood phylogenetic tree was built
701 using iqtree (v.2.2.0) (Minh et al. 2020) and the ultrafast bootstrap approximation (UFBoot)
702 method requiring a minimum of 1000 replicates (Hoang et al. 2018). The resulting tree was
703 visualized in RStudio using the ggtree R package (v.3.4.4) (Yu et al. 2017). This method was

704 also used to identify orthologous and paralogous C2H2 zinc finger transcription factors in *B.*
705 *malayi.*

706 *C. elegans* Single-cell Isolation

707 Chunks (~5 mm^2) of media from 4 day old plates were excised by flame sterilized spatula,
708 transferred to 5-10 new 10 cm NGM plates, and incubated at 20ºC. At 102-120 hr post
709 chunking, worms were washed off plates with 15 mL M9, pelleted (~1,100 rpm / 5 sec), and
710 exposed to 6 mL of freshly prepared bleaching solution (20% NaOCl, 0.5 M NaOH in ddH_2O)
711 with mild rotation until partially degraded bodies were observed (6-8 min) under Stemi 508
712 stereo-microscope. Eggs were pelleted (~1,100 rpm / 5 sec) and washed 3 x in 15 mL M9
713 media. After the final wash embryos were resuspended in 2-4 mL M9 and counted in 5 x 5 µL
714 droplets on a glass slide under a Zeiss Stemi 508 stereo-microscope. 2,000-4,000 embryos
715 were plated in 125-150 µL M9 on 20 (N2) or 55 (BK36) 10 cm NGM plates seeded with OP50
716 and kept at 20°C for 46.5 hr prior to single-cell isolation. Single-cells were isolated from bleach
717 synchronized *C. elegans* N2 and BK36 L4 stage worms using an established protocol with
718 modifications (Kaletsky et al., 2016). Worms were transferred in ~30 mL M9 media to 3 x 1.5
719 mL centrifuge tubes by sequential pelleting by microfuge followed by washing 5 x in 1.5 mL M9.
720 Worms were washed once in 500 µL lysis buffer (200 mM DTT, 0.25% SDS, 20 mM HEPES pH
721 8.0, 3% sucrose) then incubated for a further 8 min in lysis buffer with continuous rotation.
722 Digested worms were washed 5 x in M9 then subject to 500 µL pronase (20 mg/mL from
723 *Streptomyces griseus* in L-15 for 14-15 min at RT with semi-continuous pipetting. Pronase
724 treatment was stopped with FBS (3% final v/v). Large debris was pelleted by microfuge and
725 cells were filtered (7 µm nylon mesh), stained with 0.5 µg/mL DAPI, and kept on ice.
726 Throughout the protocol, samples were checked under stereo and fluorescent microscopes to
727 determine the release and integrity of cells.

728 ## FACS Pooled RNA-seq

729 FACS was performed using a FACS Aria II (Becton Dickinson) for both *C. elegans* and *B.*
730 *malayi* cell suspensions. *C. elegans* BK36 (Mattingly and Buechner, 2011) single-cell
731 suspensions generated from L4 stage larvae were sorted directly into TRIzol™ LS (Invitrogen,
732 Waltham, MA) in 1.5 mL microfuge tubes. N2 strain cells were used as reference. Gates
733 included dead cells (DAPI+, 4′,6-diamidino-2-phenylindole, 0.5 µg/mL), GFP+ cells (green
734 fluorescent protein), and cell size by aspect ratios, respectively (**Figure 3-figure supplement**
735 **2**). Total RNA was purified using Direct-zol RNA Microprep kit (Zymo Research, Irvine, CA),
736 eluted in a minimal volume of nuclease-free water and flash frozen in liquid nitrogen or dry ice
737 and stored at -80ºC. RNA integrity was determined by Agilent RNA 6000 Pico Kit (Agilent,
738 Santa Clara, CA) on a 2100 Bioanalyzer (Agilent) before library preparation. Total RNA was
739 converted to double stranded cDNA and amplified using SMART-Seq v4 (Takara, Kusatsu,
740 Shiga, Japan). Full length cDNA was quantified by 2100 Bioanalyzer (Agilent). 150 pg of
741 amplified cDNA was tagmented and index-amplified using Nextera XT adapters (Illumina).
742 Library quantity was assessed by Qubit HS DNA and quality assessed by 2100 Bioanalyzer
743 (Agilent). Libraries were then balanced and 2x75 bp sequencing was carried on the Illumina
744 MiSeq.
745
746 For *B. malayi* single-cell suspensions, gates were set to collect live single-cells (DRAQ5+,
747 DAPI-) based on size (small, large, largest), granularity, and presence or absence of
748 *Wolbachia* antibody (**Figure 3-figure supplement 1**). Presence of *Wolbachia* identified by
749 fluorescent conjugated (Lightning-Link® R-Phycoerythrin Conjugation Kit #703-0030)
750 *Wolbachia* surface protein *wBm*0432 / GenPept: WP_011256630 mouse monoclonal antibody
751 (BEI Resources, Manassas, VA). Cells were sorted into 750 uL TRIzol™ LS and libraries were
752 prepared using the NEBNext Single Cell/Low Input RNA Library Prep Kit for Illumina (NEB,

753 version 3.0, #E6420L) and NEBNext Multiplex Oligos for Illumina (Index Primers Set 1, NEB,
754 #E6440G), followed by 2x150 bp sequencing on the Illumina MiSeq. Single technical replicates
755 for *C. elegans* strains and *B. malayi* mf dispersions were completed.

756 Secretory Cell Characterization

757 Differentially expressed genes for each major annotated *B. malayi* cell type were identified
758 using the FindConservedMarkers() from the Seurat R package with an adjusted p-value less
759 than or equal to 0.05. Gene ontology (GO) IDs for annotated *B. malayi* genes were acquired
760 from WormBase ParaSite (Howe et al. 2017) using the biomaRt R package (v.2.52.0)
761 (Smedley et al. 2009) and analysis of enriched secretory cell transcripts was completed using
762 the topGO R package (v.2.48.0) (Alexa and Rahnenfuhrer 2010). Significantly enriched GO
763 terms were identified using the topGO's Fisher's exact test (p<= 0.05). The protein sequences
764 for differentially expressed secretory cell genes were obtained from WormBase and used as
765 input into SignalP 6.0 (Teufel et al., 2022) to computationally predict signal peptide sequences.
766 The "slow" model and Organism option "Other" were used as settings. Transmembrane
767 domains were predicted and quantified using the same list of differentially expressed genes for
768 each major cell type as input to HMMTOP 2.1 (Tusnády and Simon 2001).

769 Microfilariae Cell Culture

770 Single-cell suspensions for the purpose of cell culture were prepared as previously described
771 with the exception of the pronase digestion step. After the initial 30 min incubation with
772 mechanical digestion, the suspension was briefly centrifuged at 1,000 rcf to pellet undigested
773 worms. The supernatant was removed and supplemented with 1 mL L-15+10% FBS and
774 placed on ice to inhibit further pronase digestion on released single-cells. The worm pellet was
775 resuspended in an additional 100 µL of pronase (15 mg/mL) for continued digestion for 30 min

776 with manual pipetting to release cells from worms in early stages of digestion. At the end of
777 pronase digestion, all microcentrifuge tubes were centrifuged at 1,000 rcf for 6 min at 4ºC to
778 pellet undigested material and single-cells. The supernatant was replaced with L-15+10% FBS,
779 tubes were briefly centrifuged (~5 sec) and the supernatant was filtered through 7 µm mesh.
780 Peanut lectin-coated chamber slides or plates were prepared by incubating peanut lectin (0.5
781 mg/mL) (Sigma-Aldrich, St. Louis, MO) suspended in water in chamber slide wells for 30 min,
782 removed, and allowed to dry while being UV treated for 2 hr for sterilization. Filtered cell
783 suspensions were concentrated prior to plating on peanut lectin-coated chamber slides or
784 plates by centrifugation and resuspension in a smaller volume. Cells were seeded and
785 incubated in a humid chamber at 37ºC+5% CO_2. Viability was visualized using live/nucleated
786 cell staining with DRAQ5, DAPI, or Calcein-AM dyes. Two biological replicates generated from
787 microfilariae obtained from different infected jirds were completed with at least two technical
788 replicates from the same single-cell suspension dissociation reaction

789 Cell Proliferation Assay

790 *B. malayi* cell suspensions were assessed for proliferative activity using the thymidine analog
791 EdU (5-ethynyl-2'-deoxyuridine) and the Click-iT™ EdU Cell Proliferation Kit for Imaging with
792 the Alexa Fluor™ 488 dye (Thermo Fisher, Waltham, MA). Cells dissociated from *B. malayi* mf
793 were seeded onto peanut-lectin coated, UV-treated Nunc™ Lab-Tek™ II 8-well chamber slides
794 (Thermo Fisher, Waltham, MA) at a density of 30k cells/chamber in L-15+10% FBS+P/S. Cells
795 were allowed to adhere overnight at 37ºC+5% CO_2 prior to incubating in EdU at 0 µM, 0.1 µM,
796 1.0 µM, 10 µM, and 50 µM concentrations. The CHO-K1+Gα16 cell line was used as a positive
797 proliferation control to confirm the EdU Click-chemistry reaction was functioning and was
798 incubated with 0 µM and 10 µM EdU. Cells were incubated with EdU for 48 hr prior to detection
799 of EdU incorporation using the kit protocol for cell fixation, permeabilization, EdU detection, and

800 staining with Hoescht 33324 prior to imaging. Cells were imaged at 10X and 40X for CHO-
801 K1+Gα16 and B. malayi mf-derived cells, respectively.

802 Microscopy

803 Differential Interference Contrast (DIC) imaging was completed using an upright Zeiss Axio
804 Imager.D1 microscope equipped with a 100X oil objective (Plan-Neofluoar 100x, NA = 1.3 ,
805 Zeiss). All other brightfield and fluorescence microscopy used an ImageXpress Nano
806 Automated Imaging System (Molecular Devices) with 10X and 40X air objectives.

807 Integrating Model Nematode Datasets

808 In an effort to identify cell types within the *B. malayi* scRNA-seq dataset, Scanorama was used
809 as an integration tool with publicly available *C. elegans* scRNA-seq datasets based on one-to-
810 one orthologs (Hie et al., 2019). The pre-processed untreated *B. malayi* dataset was reduced
811 to only genes that have a one-to-one ortholog in *C. elegans* followed by replacement of the *B.*
812 *malayi* gene IDs to *C. elegans* gene IDs using Seurat. The Seurat object was then exported as
813 an Ann Data object for input into Scanorama. The L2 larval stage specific dataset (Ben-David
814 et al., 2020) and the most notable L4 larval stage dataset (CeNGEN) (Taylor et al., 2021) were
815 integrated with the subsetted *B. malayi* dataset with batch integration and plotted using ScanPy
816 (Wolf et al., 2018).

817 Repetitive Pipettor (ReP)

818 The ReP is an automated, 3D-printed assembly that uses a DC motor (ServoCity, Winfield,
819 KS), Raspberry Pi (rpi) Nano (CanaKit, North Vancouver, Canada), and an L298N motor
820 controller (SunFounder, Shenzhen, China) to aspirate and dispense a p200 Eppendorf
821 Research Plus pipette (Eppendorf, Hamburg, Germany) at any given rate, frequency, and

volume. The structure was designed and modeled in Solidworks 2020 (https://www.solidworks.com/). The design includes six independent parts that were converted to STL files in Solidworks and sliced in Ultimaker Cura (https://github.com/Ultimaker/Cura) using the default printing settings of 0.2 mm layer height, 20% infill, and support material checked. The flat face of each part was positioned in contact with the build plate to reduce support material and refine rounded surfaces. Parts were printed using polylactic acid plastic filament and the support material was removed prior to assembly. Four pins were soldered to the rpi at pin locations 16, 18, 20, and 22. The rpi was subsequently glued to the 3D-printed structure at the four corner supports such that the SD card was facing upwards, and the USB and HDMI ports were facing outwards. The LN298 motor controller was glued to the opposite side of the structure such that the heat sink was facing downwards. For the rpi, ports 16, 18, and 22 were general purpose input/output pins and were connected to the IN1, IN2, and ENA ports of the motor controller, respectively. Port 20 was a ground inserted at the GND port of the motor controller. The 12-volt power supply had a positive and negative lead inserted into the motor controller at the +12V and GND ports, respectively. The OUT1 and OUT2 ports on the motor controller were finally wired and soldered to the motor terminals. All code was written in python, and the rpi was controlled remotely via SSH tunnels. All part files, protocol codes, and in-depth fabrication instructions can be found at https://github.com/emmakn/ReP.

Acknowledgements

The authors would like to thank the University of Wisconsin Carbone Cancer Center (UWCCC) Flow Lab and the Cancer Center Support Grant P30 CA014520 for assistance with flow cytometry. The UWCCCC Cytek Aurora Spectral Cytometer was made available through a NIH Shared Instrumentation Grant (Grant #: 1S10OD025225-01, Project Title: BD FACSymphony High Parameter Flow Cytometer). The authors would also like to thank the University of

Wisconsin Biotechnology Center Gene Expression Center for facilitating single-cell and low-input RNA-sequencing. *Brugia* life cycle stages were obtained through the NIH/NIAID Filarial Research Reagent Resource Center (FR3), morphological voucher specimens are stored at the Harold W. Manter Museum at University of Nebraska, accession numbers P2021-2032. *C. elegans* strains were provided by the CGC, which is funded by NIH Office of Research Infrastructure Programs (P40 OD010440). Finally, the authors would like to thank Gabi Munoz for help optimizing single-cell suspensions and members of the Zamanian lab for constructive comments on the manuscript.

Funding

This work was supported by National Institutes of Health NIAID grant R01 AI151171 to MZ and the Wisconsin Alumni Research Foundation (WARF).

Competing Interests

The authors have declared no competing interests exist.

Figures

Figure 1

Optimization of single-cell dissociation in *B. malayi* microfilariae.

(**A**) Schematic of dissociation protocol using 1 million *B. malayi* microfilariae as input. (**B**) Images of 96-well plate wells containing pre- and post- PD-10 filtration of microfilariae-containing peritoneal lavage. Unfiltered solutions (left) contain a plethora of host cell and tissue contamination and parasite embryos. Filtered solutions (right) minimize host contamination carryover prior to cell dissociation and downstream applications. (**C**) Representative Giemsa

867 stained microfilariae pre-chitinase (left) and post-chitinase (right) treatment. Chitinase disrupts
868 sheath integrity visible in the head (white arrows) and tail spaces (black arrows). Scale bar =
869 100 µm. (**D**) Cell dissociation timelapse during pronase digestion and mechanical disruption.
870 Scale bar = 50 µm. (**E**) High content imaging flow cytometry of single-cell suspensions. Left:
871 Gating scheme to identify objects based on nucleation (DRAQ5+ stain) and high viability
872 (Calcein-AM+ stain). Objects colored in green indicate highly viable, nucleated objects carried
873 forward in the downstream analysis. Right: Single-cell objects were segregated by IDEAS
874 software and objects with aspect ratios >= 0.8 for brightfield and DRAQ5 channels were
875 counted as single-cells (blue). A mixed population (grey) included objects belonging to
876 doublets/multiples/debris (orange). All captured images were scanned by eye for cells with ES-
877 like morphology (black) and included as single-cells. Bottom: Representative images of cells
878 belonging to the identified single-cell (blue), mixed (grey), ES-like (black), and multiplet/debris
879 (orange) populations. Scale bars = 10 µm.
880

881 Figure 2

882 **A single-cell transcriptomic atlas of *B. malayi* microfilariae cell types.**
883 (**A**) Global UMAP transcriptome clustering of 46,621 cells with cell type annotations. Inset:
884 Comparison of bulk transcript per million counts (tpm) (Bulk: Log_{10}(tpm)) and single-cell RNA-
885 seq total read counts (SC: Log_{10}(Total)) indicates the transcriptomic profile of the single-cell
886 atlas largely recapitulates the gene expression profile of bulk tissue RNA-sequencing.
887 Correlation between the bulk and single-cell RNA-seq datasets was assessed using Pearson
888 correlation coefficient. Linear model regression line is indicated in red. (**B**) Gene expression
889 distribution (color) and proportion of cells per cluster (size) expressing neurotransmitter-specific
890 genes. Clusters 24 and 25 are aminergic and cluster 26 is GABAergic. Glutamatergic and

891 cholinergic neurons are unresolved. MS=Muscle, MD=Mesoderm, C=Coelomocyte,
892 S=Secretory, CA=Canal-associated, IB=Inner body.

893 Figure 3

894 **Annotation of the *Brugia* secretory cell and localization of secretory-related antigens**
895 **indicates broad distribution of antigen transcriptic origins.**
896 (**A**) Schematic of FACS enrichment approach for isolating cell populations in *B. malayi* mf
897 single-cell dispersions. Viable cells were sorted by size, granularity and the presence or
898 absence of anti-*Wolbachia* fluorescent antibodies and collected directly into TRIzol LS^{TM} for
899 RNA isolation and sequencing. (**B**) Differentially expressed genes in the "Largest" cells sample,
900 the population hypothesized to contain the secretory cell, were projected on the mf single-cell
901 atlas and indicated expression enrichment in cluster 15. Read count represents summed reads
902 across mapped genes in the single-cell atlas. (**C**) Cell and marker coexpression quantification
903 in cells belonging to cluster 15 using the DEGs identified in Figure 3A. Cluster 15 includes the
904 majority of cells expressing DEGs and contains the most cells coexpressing 2 or more
905 markers. (**D**) Single-cell suspension of *C. elegans* strain BK36 with the excretory canal
906 cytoplasm labeled with GFP. Heatmap representing differential gene expression from sorted
907 cell populations by FACS based on size and GFP(+/-) expression. (**E**) Dot plot of secreted,
908 diagnostic, and vaccine antigens grouped by annotated cell type. Color indicates average gene
909 expression per cluster. Circle diameter denotes proportion of cells in each cluster expressing
910 the indicated gene. Presence of a blue box indicates whether the resultant protein from the
911 gene is considered an abundant secretory antigen, a diagnostic antigen (Diagnos.) or whether
912 the resulting protein has been investigated as a vaccine target (Vacc.). MS=Muscle,
913 MD=Mesoderm, C=Coelomocyte, S=Secretory, CA=Canal-associated, IB=Inner body.

914 Figure 4

915 **Characterization of the secretory cell indicates an enrichment in signal peptide**
916 **containing proteins and C2H2 zinc finger transcription factors**.
917 (**A**) Quantification of signal peptide-containing sequences among all DEGs (p <= 0.05) across
918 major annotated cell types. Differentially expressed transcripts in the secretory cell show an
919 enrichment for signal peptide sequences. S=Secretory, MS=Muscle, MD=Mesoderm,
920 C=Coelomocyte, CA=Canal-associated, IB=Inner body, N=Neurons. (**B**) Quantification of
921 transmembrane domains of differentially expressed transcripts in the secretory cell. Secretory
922 cells contain several genes with a single predicted transmembrane domain but very few
923 proteins contain more than one domain. (**C**) Phylogenetic and expression analysis of C2H2
924 zinc finger transcription factors in *B. malayi* (red) based on orthologous C2H2-ZF TFs
925 confirmed through direct evidence in *C. elegans* (black). Paralogous expansion (red boxes) of
926 these transcription factors is observed with nearly exclusive expression in the secretory cell.
927 A summary of gene ontology (GO) enrichment for differentially expressed genes of the
928 secretory cell can be found in **Figure 4-figure supplement 1**.

929 Figure 5

930 **Distribution of putative anthelmintic targets and ligand-gated ion channel subunit**
931 **colocalization.**
932 (**A**) Transcriptomic and gene expression profiles of major anthelmintic targets in microfilarial
933 cell types. Targets include β-tubulins and cys-loop ligand-gated ion channel (LGIC) subunits
934 corresponding to the following subfamilies: big potassium (BK), G protein-coupled receptor
935 (GPCR), glutamate-gated chloride channel (GluCl), acetylcholine-gated channel (ACC),
936 nicotinic acetylcholine receptor (nAChR), transient receptor potential channel (TRP), and cyclic
937 nucleotide-gated ion channels (CNG). (**B**) UMAP depiction of cells expressing putative targets

938 of benzimidazoles (β-tubulins), emodepside (*slo-1*), and macrocyclic lactones (GluCls). (**C**)
939 Phylogenetic trees showing single-cell correlations between subunits belonging to GluCl and
940 nAChR LGIC subfamilies and β-tubulins. Empty circles represent *C. elegans* and filled circles
941 represent *B. malayi*. Red links indicate positive Pearson correlation coefficients calculated
942 using the log normalized count values. MS=Muscle, MD=Mesoderm, C=Coelomocyte,
943 S=Secretory, CA=Canal-associated, IB=Inner body.

944 Figure 6

945 **Cell viability and transcriptional shifts in response to anthelmintics.**
946 (**A**) Schematic and representative flow cytometry contour plots depicting Calcein Violet-AM
947 (viable) fluorescence in control samples (untreated, 0.1% DMSO, and methanol fixed).
948 Methanol fixed cells show no retention of Calcein Violet-AM indicated by decreased
949 fluorescence in the violet channel. (**B**) Viability of dispersed cell suspensions incubated on ice
950 for 8 hr. Significant variation in the percent viability of cell populations after dissociation was
951 observed and attributed to the variation in mf health prior to dispersion as well as small
952 nuances in pronase digestion. (**C**) Drug dose response curves on dispersed single-cell
953 suspensions at 50 nM, 1 μM, 50 μM, 100 μM, and a DMSO-only (0.1%) control. Viability was
954 normalized to the percent DMSO control. AZS = albendazole sulfoxide, LEV = levamisole, IVM
955 = ivermectin. Black line indicates the average of three biological replicates for IVM and two
956 biological replicates for LEV and AZS. Red line indicates the EC_{50} value for IVM at 51 ± 5.16
957 μM. (**D**) Representative flow cytometry contour plots of cell viability in response to IVM
958 treatment. A decrease in Calcein Violet-AM fluorescence at 50 μM and nearly total cell death at
959 100 μM. (**E**) Left: Single-cell transcriptomic response to IVM treatment (1 μM for 20 min, 1%
960 DMSO). UMAP plot showing treated (top) and untreated (bottom) clustering of cell types.
961 Middle: Volcano plots depicting differentially expressed genes (DEGs) in treated and untreated
962 groups by cell type annotations. DEGs were calculated using Seurat's FindMarkers() function

963 and comparing treated vs untreated clusters. Orange color indicates upregulation in IVM-
964 treated cells. Right: Volcano plot of differentially expressed genes colored by cluster.

965 Figure 7

966 **Cells of dispersed microfilaria are viable in culture 96 hr after dissociation.**
967 (**A**) DIC and fluorescence microscopy of cells from microfilarial stage *B. malayi* parasites on
968 peanut-lectin coated slides after 24 hr incubation in culture medium. The cell population
969 contains a range of cell sizes including single-cells and clustered cells and a subset of the cell
970 population have protrusions indicating a muscle or neuronal cell type. Calcein fluorescence
971 (live) with varying intensities of brightness indicates a range of viability among the cell
972 population. Scale bar = 20 µm. (**B**) Quantification of cell viability over a period of 96 hr using
973 DRAQ5 and Calcein-AM viability dyes. Black line represents the mean and standard error of
974 viability per replicate.

975 Supplemental Figure Legends

976 **Figure 1-figure supplement 1** - Optimization of SDS-DTT incubation by time and
977 concentration.
978
979 **Figure 1-source data 1** - Comparison of cell counting methods by hemocytometer, flow
980 cytometry, and automated cell counting instrument. Determining the total cell count in the
981 suspension was difficult due to remnants of debris and small and variable sized cells within the
982 suspension. The recommended tabletop automated cell counting system Countess II (Thermo
983 Fisher, Waltham, MA) was unreliable in confirming total and viable cell counts, likely due to cell
984 sizes below the lower threshold of the instrument and because the cells are in multiple focal
985 planes within the chip. Fluorescent activated cell sorting (FACS) was also used to estimate cell

986 count and to attempt enrichment of viable cells prior to loading the 10x Genomics. The majority
987 of cells did not survive the FACS process and could not be recovered for input into the 10x
988 Genomics Chromium controller. Estimating cell concentration was most reliable using a
989 hemocytometer. Bpa = *Brugia pahangi*; Bma = *Brugia malayi*; mf = microfilariae
990
991 **Figure 2-figure supplement 1** - Histograms of genes (left) and UMIs (right) per cell across all
992 clustered cells. Red line indicates the mean.
993
994 **Figure 2-figure supplement 2** - (**A**) Dot plot of orthologous *B. malayi* transcription factors
995 based on *C. elegans* transcription factors confirmed through direct evidence as indicated in the
996 CIS-BP database. Dot size indicates the proportion of cells within the corresponding cluster
997 expressing the gene and the color represents the average level of expression across the
998 expressing cells in the cluster. MS=Muscle, MD=Mesoderm, C=Coelomocyte, S=Secretory,
999 CA=Canal-associated, IB=Inner body (**B**) UMAP representation of ciliated sensory neuron
1000 specific transcription factor *Bma-daf-19* and genes that contribute to ciliogenesis. Intraflagellar
1001 transport (IFT) represented by *Bma-che-3.1, Bma-che-3.2, Bma-xbx-1, Bma-dylt-2, Bma-che-*
1002 *11, Bma-daf-10, Bma-osm-5, Bma-ift-81, Bma-ift-74, Bma-osm-6, Bma-osm-1, Bma-che-2*,
1003 *Bma-che-13*. Kinesin-II IFT motors represented by *Bma-klp-11, Bma-klp-20, and Bma-kap-1*.
1004 Bardet-Biedl Syndrome (BBS) stabilizing proteins represented by *Bma-bb-1, Bma-bbs-2.1,*
1005 *Bma-bbs-2.2, Bm4542, Bma-bbs-5, Bma-osm-12, Bma-bbs-8,* and *Bma-bbs-9*.
1006
1007 **Figure 2-figure supplement 3** - UMAP visualization of marker genes used to annotate cell
1008 type clusters.
1009
1010 **Figure 2-figure supplement 4** - Pseudobulk analysis of scRNA-seq transcriptomic data. The
1011 raw counts for each cluster based on treatment (untreated or IVM-treated) were aggregated to

1012 simulate a bulk transcriptomic library sample. Samples and *B. malayi* genes are hierarchically
1013 clustered to show samples that represent similar cell types and differentially expressed genes
1014 across cell types.
1015
1016 **Figure 2-figure supplement 5** - Distribution of neuronal gene transcripts across all clusters.
1017 Circle size (Total reads (%)) represents the proportion of total reads for each gene located in
1018 that cluster. Color indicates neuronal class. MS=Muscle, MD=Mesoderm, C=Coelomocyte,
1019 S=Secretory, CA=Canal-associated, IB=Inner body.
1020
1021 **Figure 2-figure supplement 6** - Integration of single-cell datasets using Scanorama algorithm.
1022 Bma = *B. malayi* mf. Ben-David = *C. elegans* L2 stage dataset from Ben-David et al. (2020).
1023 CeNGEN = *C. elegans* L4 stage from Taylor et al. (2021). Integration of the three datasets
1024 using the Scanorama algorithm is colored by dataset (A) and annotated cell type (B).
1025
1026 **Figure 3-figure supplement 1** - Representative FACS gating scheme for collecting *B. malayi*
1027 single-cells based on size, granularity, and presence or absence of anti-*Wolbachia* IgG
1028 antibody. Cells were separated from debris (Gate 1) and live single-cells were differentiated
1029 from doublets using forward scatter, side scatter, and DAPI/DRAQ5 staining (Gates 2-4). Cells
1030 were further separated based on increased granularity (Gate 5B), increased cell size (Gate
1031 5C), or small, round cells (Gate 5A). Small, round cells were further separated by the presence
1032 or absence of anti-*Wolbachia* IgG antibody binding (Gate 6 A1 and Gate 6A2, respectively).
1033
1034 **Figure 3-figure supplement 2** - Representative FACS gating scheme for collecting *C. elegans*
1035 strain BK36 cell populations. Cells were separated from debris (Gate 1) and live single-cells
1036 differentiated from doublets using forward scatter, side scatter, and DAPI intensity (Gates 2-4).

1037 GFP(-) cells were separated for collection (Gate 5) and GFP(+) cells were further separated by
1038 size based on forward scatter and collected as small and large cell populations (Gate 6).
1039
1040 **Figure 3-figure supplement 3** - Distribution of gene transcripts across all clusters. Circle size
1041 (Total reads (%)) represents the proportion of total reads for each gene located in the specified
1042 cluster. Transcript abundance distribution across cell types for prominent antigens.
1043 MS=Muscle, MD=Mesoderm, C=Coelomocyte, S=Secretory, CA=Canal-associated, IB=Inner
1044 body.
1045
1046 **Figure 3-source data 1** - List of differentially expressed genes identified in the *B. malayi* mf
1047 "largest" cell population collected via FACS and bulk RNA-seq.
1048
1049 **Figure 3-source data 2** - List of differentially expressed genes in secretory cells (cluster 15).
1050 Differentially expressed genes associated with secretory cells (cluster 15)
1051
1052 **Figure 3-source data 3** - List of differentially expressed genes identified in *C. elegans* large
1053 and GFP(+) cells collected via FACS and bulk RNA-seq.
1054
1055 **Figure 3-source data 4** - Comprehensive table of major antigens, vaccine targets, diagnostic
1056 markers, and notable secreted proteins.
1057
1058 **Figure 4-figure supplement 1** - Gene Ontology (GO) term enrichment analysis for
1059 differentially expressed genes identified in the secretory cell.
1060
1061 **Figure 4-source data 1** - Summary table of signal peptide sequence predictions in
1062 differentially expressed transcripts across major annotated cell types. S=Secretory,

1063 MS=Muscle, MD=Mesoderm, C=Coelomocyte, CA=Canal-associated, IB=Inner body,
1064 N=Neurons.
1065
1066 **Figure 4-source data table 2 -** Summary of transmembrane domain prediction in differentially
1067 expressed transcripts across major annotated cell types. S=Secretory, MS=Muscle,
1068 MD=Mesoderm, C=Coelomocyte, CA=Canal-associated, IB=Inner body, N=Neurons.
1069
1070 **Figure 5-figure supplement 1** - Distribution of gene transcripts associated with anthelmintic
1071 targets across all cell clusters. Circle size (Total reads (%)) represents the proportion of total
1072 reads for each gene located in the specified cluster. MS=Muscle, MD=Mesoderm,
1073 C=Coelomocyte, S=Secretory, CA=Canal-associated, IB=Inner body.
1074
1075 **Figure 6-source data 1** - Differential gene expression analysis between untreated and IVM (1
1076 μM) treated single-cell suspensions. Positive average log_2 fold-change (avg_log2FC) values
1077 indicate the gene is more highly expressed in cells exposed to IVM. Pct.1 and pct.2 correspond
1078 to the percentage of cells expressing the gene in the treated and untreated cell populations,
1079 respectively. P-values were adjusted (p_val_adj) using a Bonferroni p-value correction
1080 approach.
1081
1082 **Figure 7-figure supplement 1** - Representative images of cell viability over 96 hr. DRAQ5
1083 (red) indicates nucleated objects and Calcein-AM (green) fluorescence indicates viable cells.
1084 Scale bar = 20 μm.
1085
1086 **Figure 7-figure supplement 2** - EdU cell proliferation assay of *B. malayi* mf-derived cells and
1087 CHO-K1+Gα16 cells as a proliferating cell positive control. *B. malayi* cells were incubated with
1088 different EdU concentrations and EdU was detected using an anti-EdU Alexa Fluor 488 azide.

1089 No EdU incorporation is detected in the *B. malayi* cells indicating the dissociated cell

1090 suspensions are not proliferative in culture. Scale bars are 50 μm and 10 μm for CHO-

1091 K1+Gα16 and *B. malayi* cells, respectively.

1092 # References

1093 A. F. Bird JB. 1991. Secretory-Excretory System In: Bird AF, Bird J, editors. The Structure of
1094 Nematodes (Second Edition). San Diego: Academic Press, Inc. pp. 167–182.
1095 doi:10.1016/B978-0-12-099651-3.50015-0

1096 Airs PM, Vaccaro K, Gallo KJ, Dinguirard N, Heimark ZW, Wheeler NJ, He J, Weiss KR,
1097 Schroeder NE, Huisken J, Zamanian M. 2022. Spatial transcriptomics reveals antiparasitic
1098 targets associated with essential behaviors in the human parasite Brugia malayi. *PLoS*
1099 *Pathog* **18**:e1010399. doi:10.1371/journal.ppat.1010399

1100 Ballesteros C, Tritten L, O'Neill M, Burkman E, Zaky WI, Xia J, Moorhead A, Williams SA,
1101 Geary TG. 2016. The Effects of Ivermectin on Brugia malayi Females In Vitro: A
1102 Transcriptomic Approach. *PLoS Negl Trop Dis* **10**:e0004929.
1103 doi:10.1371/journal.pntd.0004929

1104 Ben-David E, Boocock J, Guo L, Zdraljevic S, Bloom JS, Kruglyak L. 2020. Whole-organism
1105 mapping of the genetics of gene expression at cellular resolution. *bioRxiv*.
1106 doi:10.1101/2020.08.23.263798

1107 Bennuru S, Meng Z, Ribeiro JMC, Semnani RT, Ghedin E, Chan K, Lucas DA, Veenstra TD,
1108 Nutman TB. 2011. Stage-specific proteomic expression patterns of the human filarial
1109 parasite Brugia malayi and its endosymbiont Wolbachia. *Proc Natl Acad Sci U S A*
1110 **108**:9649–9654. doi:10.1073/pnas.1011481108

1111 Campbell WC. 1982. Efficacy of the avermectins against filarial parasites: a short review. *Vet*
1112 *Res Commun* **5**:251–262.

1113 Cao J, Packer JS, Ramani V, Cusanovich DA, Huynh C, Daza R, Qiu X, Lee C, Furlan SN,
1114 Steemers FJ, Adey A, Waterston RH, Trapnell C, Shendure J. 2017. Comprehensive
1115 single-cell transcriptional profiling of a multicellular organism. *Science* **357**:661–667.

1116 doi:10.1126/science.aam8940
1117 Chippaux JP, Boussinesq M, Gardon J, Gardon-Wendel N, Ernould JC. 1996. Severe adverse
1118 reaction risks during mass treatment with ivermectin in loiasis-endemic areas. *Parasitol*
1119 *Today* **12**:448–450. doi:10.1016/0169-4758(96)40006-0
1120 Chitwood and Chitwood. 1950. The Excretory SystemAn Introduction to Nematology. pp. 126–
1121 135.
1122 Choi Y-J, Ghedin E, Berriman M, McQuillan J, Holroyd N, Mayhew GF, Christensen BM,
1123 Michalski ML. 2011. A deep sequencing approach to comparatively analyze the
1124 transcriptome of lifecycle stages of the filarial worm, Brugia malayi. *PLoS Negl Trop Dis*
1125 **5**:e1409. doi:10.1371/journal.pntd.0001409
1126 Choudhary S, Abongwa M, Kashyap SS, Verma S, Mair GR, Kulke D, Martin RJ, Robertson
1127 AP. 2022. Nodulisporic acid produces direct activation and positive allosteric modulation of
1128 AVR-14B, a glutamate-gated chloride channel from adult Brugia malayi. *Proc Natl Acad*
1129 *Sci U S A* **119**:e2111932119. doi:10.1073/pnas.2111932119
1130 Dent JA, Smith MM, Vassilatis DK, Avery L. 2000. The genetics of ivermectin resistance in
1131 Caenorhabditis elegans. *Proc Natl Acad Sci U S A* **97**:2674–2679.
1132 doi:10.1073/pnas.97.6.2674
1133 Fuhrman JA, Piessens WF. 1985. Chitin synthesis and sheath morphogenesis in Brugia malayi
1134 microfilariae. *Mol Biochem Parasitol* **17**:93–104. doi:10.1016/0166-6851(85)90130-6
1135 Galal M, Fujimaki Y, Shimada M, Aoki Y. 1989. Comparison of the Methods Available for
1136 Purification of Brugia pahangi Microfilariae in the Peritoneal Lavage of Jirds (Meriones
1137 unguiculatus). *Tropical Medicine* **31**:103–109.
1138 Geary TG, Bourguinat C, Prichard RK. 2011. Evidence for macrocyclic lactone anthelmintic
1139 resistance in Dirofilaria immitis. *Top Companion Anim Med* **26**:186–192.
1140 doi:10.1053/j.tcam.2011.09.004
1141 Geary TG, Woo K, McCarthy JS, Mackenzie CD, Horton J, Prichard RK, de Silva NR, Olliaro

1142 PL, Lazdins-Helds JK, Engels DA, Bundy DA. 2010a. Unresolved issues in anthelmintic
1143 pharmacology for helminthiases of humans. *Int J Parasitol* **40**:1–13.
1144 doi:10.1016/j.ijpara.2009.11.001
1145 Geary TG, Woo K, McCarthy JS, Mackenzie CD, Horton J, Prichard RK, de Silva NR, Olliaro
1146 PL, Lazdins-Helds JK, Engels DA, Bundy DA. 2010b. Unresolved issues in anthelmintic
1147 pharmacology for helminthiases of humans. *Int J Parasitol* **40**:1–13.
1148 doi:10.1016/j.ijpara.2009.11.001
1149 Greene SE, Fischer K, Choi Y-J, Curtis KC, Budge PJ, Mitreva M, King CL, Fischer PU, Weil
1150 GJ. 2022. Characterization of a novel microfilarial antigen for diagnosis of Wuchereria
1151 bancrofti infections. *PLoS Negl Trop Dis* **16**:e0010407. doi:10.1371/journal.pntd.0010407
1152 Hao Y, Hao S, Andersen-Nissen E, Mauck WM 3rd, Zheng S, Butler A, Lee MJ, Wilk AJ, Darby
1153 C, Zager M, Hoffman P, Stoeckius M, Papalexi E, Mimitou EP, Jain J, Srivastava A, Stuart
1154 T, Fleming LM, Yeung B, Rogers AJ, McElrath JM, Blish CA, Gottardo R, Smibert P, Satija
1155 R. 2021. Integrated analysis of multimodal single-cell data. *Cell* **184**:3573–3587.e29.
1156 doi:10.1016/j.cell.2021.04.048
1157 Harischandra H, Yuan W, Loghry HJ, Zamanian M, Kimber MJ. 2018. Profiling extracellular
1158 vesicle release by the filarial nematode Brugia malayi reveals sex-specific differences in
1159 cargo and a sensitivity to ivermectin. *PLoS Negl Trop Dis* **12**:e0006438.
1160 doi:10.1371/journal.pntd.0006438
1161 Harnett W. 2014. Secretory products of helminth parasites as immunomodulators. *Mol*
1162 *Biochem Parasitol* **195**:130–136. doi:10.1016/j.molbiopara.2014.03.007
1163 Hewitson JP, Harcus YM, Curwen RS, Dowle AA, Atmadja AK, Ashton PD, Wilson A, Maizels
1164 RM. 2008. The secretome of the filarial parasite, Brugia malayi: proteomic profile of adult
1165 excretory-secretory products. *Mol Biochem Parasitol* **160**:8–21.
1166 doi:10.1016/j.molbiopara.2008.02.007
1167 Hie B, Bryson B, Berger B. 2019. Efficient integration of heterogeneous single-cell

1168 transcriptomes using Scanorama. *Nat Biotechnol* **37**:685–691. doi:10.1038/s41587-019-
1169 0113-3
1170 Higazi TB, Merriweather A, Shu L, Davis R, Unnasch TR. 2002. Brugia malayi: transient
1171 transfection by microinjection and particle bombardment. *Exp Parasitol* **100**:95–102.
1172 doi:10.1016/S0014-4894(02)00004-8
1173 Higazi TB, Shu L, Unnasch TR. 2004. Development and transfection of short-term primary cell
1174 cultures from Brugia malayi. *Mol Biochem Parasitol* **137**:345–348.
1175 doi:10.1016/j.molbiopara.2004.06.004
1176 Hotterbeekx A, Perneel J, Vieri MK, Colebunders R, Kumar-Singh S. 2021. The secretome of
1177 filarial nematodes and its role in host-parasite interactions and pathogenicity in
1178 onchocerciasis-associated epilepsy. *Front Cell Infect Microbiol* **11**:662766.
1179 doi:10.3389/fcimb.2021.662766
1180 Ismail M, Botros S, Metwally A, William S, Farghally A, Tao LF, Day TA, Bennett JL. 1999.
1181 Resistance to praziquantel: direct evidence from Schistosoma mansoni isolated from
1182 Egyptian villagers. *Am J Trop Med Hyg* **60**:932–935. doi:10.4269/ajtmh.1999.60.932
1183 Kaletsky R, Lakhina V, Arey R, Williams A, Landis J, Ashraf J, Murphy CT. 2016. The C.
1184 elegans adult neuronal IIS/FOXO transcriptome reveals adult phenotype regulators.
1185 *Nature* **529**:92–96. doi:10.1038/nature16483
1186 Kalyanasundaram R, Khatri V, Chauhan N. 2020. Advances in Vaccine Development for
1187 Human Lymphatic Filariasis. *Trends Parasitol* **36**:195–205. doi:10.1016/j.pt.2019.11.005
1188 Kang JS, Kim JS. 2000. Zinc finger proteins as designer transcription factors. *J Biol Chem*
1189 **275**:8742–8748. doi:10.1074/jbc.275.12.8742
1190 Kashyap SS, Verma S, Voronin D, Lustigman S, Kulke D, Robertson AP, Martin RJ. 2019.
1191 Emodepside has sex-dependent immobilizing effects on adult Brugia malayi due to a
1192 differentially spliced binding pocket in the RCK1 region of the SLO-1 K channel. *PLoS*
1193 *Pathog* **15**:e1008041. doi:10.1371/journal.ppat.1008041

1194 Kaushal NA, Hussain R, Nash TE, Ottesen EA. 1982. Identification and characterization of
1195 excretory-secretory products of Brugia malayi, adult filarial parasites. *J Immunol* **129**:338–
1196 343.
1197 Krause M, Harrison SW, Xu SQ, Chen L, Fire A. 1994. Elements regulating cell- and stage-
1198 specific expression of the C. elegans MyoD family homolog hlh-1. *Dev Biol* **166**:133–148.
1199 doi:10.1006/dbio.1994.1302
1200 Krushna NSA, Shiny C, Dharanya S, Sindhu A, Aishwarya S, Narayanan RB. 2009.
1201 Immunolocalization and serum antibody responses to Brugia malayi pepsin inhibitor
1202 homolog (Bm-33). *Microbiol Immunol* **53**:173–183. doi:10.1111/j.1348-0421.2009.00114.x
1203 Lalitha P, Eswaran D, Gnanasekar M, Rao KVN, Narayanan RB, Scott A, Nutman T, Kaliraj P.
1204 2002. Development of antigen detection ELISA for the diagnosis of brugian and
1205 bancroftian filariasis using antibodies to recombinant filarial antigens Bm-SXP-1 and Wb-
1206 SXP-1. *Microbiol Immunol* **46**:327–332. doi:10.1111/j.1348-0421.2002.tb02703.x
1207 Lamassiaude N, Courtot E, Corset A, Charvet CL, Neveu C. 2022. Pharmacological
1208 characterization of novel heteromeric GluCl subtypes from Caenorhabditis elegans and
1209 parasitic nematodes. *Br J Pharmacol* **179**:1264–1279. doi:10.1111/bph.15703
1210 Landmann F, Foster JM, Slatko B, Sullivan W. 2010. Asymmetric Wolbachia segregation
1211 during early Brugia malayi embryogenesis determines its distribution in adult host tissues.
1212 *PLoS Negl Trop Dis* **4**:e758. doi:10.1371/journal.pntd.0000758
1213 Li BW, Rush AC, Weil GJ. 2014. High level expression of a glutamate-gated chloride channel
1214 gene in reproductive tissues of Brugia malayi may explain the sterilizing effect of
1215 ivermectin on filarial worms. *Int J Parasitol Drugs Drug Resist* **4**:71–76.
1216 doi:10.1016/j.ijpddr.2014.01.002
1217 Lightowlers MW, Rickard MD. 1988. Excretory-secretory products of helminth parasites: effects
1218 on host immune responses. *Parasitology* **96 Suppl**:S123–66.
1219 doi:10.1017/s0031182000086017

1220 Liu C, Grote A, Ghedin E, Unnasch TR. 2020. CRISPR-mediated Transfection of Brugia
1221 malayi. *PLoS Negl Trop Dis* **14**:e0008627. doi:10.1371/journal.pntd.0008627
1222 Liu C, Mhashilkar AS, Chabanon J, Xu S, Lustigman S, Adams JH, Unnasch TR. 2018.
1223 Development of a toolkit for piggyBac-mediated integrative transfection of the human
1224 filarial parasite Brugia malayi. *PLoS Negl Trop Dis* **12**:e0006509.
1225 doi:10.1371/journal.pntd.0006509
1226 Local Burden of Disease 2019 Neglected Tropical Diseases Collaborators. 2020. The global
1227 distribution of lymphatic filariasis, 2000-18: a geospatial analysis. *Lancet Glob Health*
1228 **8**:e1186–e1194. doi:10.1016/S2214-109X(20)30286-2
1229 Loghry HJ, Yuan W, Zamanian M, Wheeler NJ, Day TA, Kimber MJ. 2020. Ivermectin inhibits
1230 extracellular vesicle secretion from parasitic nematodes. *J Extracell Vesicles* **10**:e12036.
1231 doi:10.1002/jev2.12036
1232 Maizels RM, Gomez-Escobar N, Gregory WF, Murray J, Zang X. 2001. Immune evasion genes
1233 from filarial nematodes. *Int J Parasitol* **31**:889–898. doi:10.1016/s0020-7519(01)00213-2
1234 Mattingly BC, Buechner M. 2011. The FGD homologue EXC-5 regulates apical trafficking in C.
1235 elegans tubules. *Dev Biol* **359**:59–72. doi:10.1016/j.ydbio.2011.08.011
1236 McInnes L, Healy J, Saul N, Großberger L. 2018. UMAP: Uniform Manifold Approximation and
1237 Projection. *J Open Source Softw* **3**:861. doi:10.21105/joss.00861
1238 McLaren DJ. 1972. Ultrastructural studies on microfilariae (Nematoda: Filarioidea).
1239 *Parasitology* **65**:317–332. doi:10.1017/s0031182000045108
1240 Michalski ML, Griffiths KG, Williams SA, Kaplan RM, Moorhead AR. 2011. The NIH-NIAID
1241 Filariasis Research Reagent Resource Center. *PLoS Negl Trop Dis* **5**:e1261.
1242 doi:10.1371/journal.pntd.0001261
1243 Moreno Y, Geary TG. 2008. Stage- and gender-specific proteomic analysis of Brugia malayi
1244 excretory-secretory products. *PLoS Negl Trop Dis* **2**:e326.
1245 doi:10.1371/journal.pntd.0000326

1246 Moreno Y, Geary TG, Tritten L. 2021. When Secretomes Meet Anthelmintics: Lessons for
1247 Therapeutic Interventions. *Trends Parasitol* **37**:468–475. doi:10.1016/j.pt.2021.01.007
1248 Moreno Y, Nabhan JF, Solomon J, Mackenzie CD, Geary TG. 2010. Ivermectin disrupts the
1249 function of the excretory-secretory apparatus in microfilariae of Brugia malayi. *Proc Natl*
1250 *Acad Sci U S A* **107**:20120–20125. doi:10.1073/pnas.1011983107
1251 Morris CP, Bennuru S, Kropp LE, Zweben JA, Meng Z, Taylor RT, Chan K, Veenstra TD,
1252 Nutman TB, Mitre E. 2015. A Proteomic Analysis of the Body Wall, Digestive Tract, and
1253 Reproductive Tract of Brugia malayi. *PLoS Negl Trop Dis* **9**:e0004054.
1254 doi:10.1371/journal.pntd.0004054
1255 Morris CP, Evans H, Larsen SE, Mitre E. 2013. A comprehensive, model-based review of
1256 vaccine and repeat infection trials for filariasis. *Clin Microbiol Rev* **26**:381–421.
1257 doi:10.1128/CMR.00002-13
1258 Mutafchiev Y, Bain O, Williams Z, McCall JW, Michalski ML. 2014. Intraperitoneal development
1259 of the filarial nematode Brugia malayi in the Mongolian jird (Meriones unguiculatus).
1260 *Parasitol Res* **113**:1827–1835. doi:10.1007/s00436-014-3829-5
1261 Nelson FK, Riddle DL. 1984. Functional study of the Caenorhabditis elegans secretory-
1262 excretory system using laser microsurgery. *J Exp Zool* **231**:45–56.
1263 doi:10.1002/jez.1402310107
1264 Ni Z, Chen S, Brown J, Kendziorski C. 2020. CB2 improves power of cell detection in droplet-
1265 based single-cell RNA sequencing data. *Genome Biol* **21**:137. doi:10.1186/s13059-020-
1266 02054-8
1267 Osei-Atweneboana MY, Awadzi K, Attah SK, Boakye DA, Gyapong JO, Prichard RK. 2011.
1268 Phenotypic evidence of emerging ivermectin resistance in Onchocerca volvulus. *PLoS*
1269 *Negl Trop Dis* **5**:e998. doi:10.1371/journal.pntd.0000998
1270 Packer JS, Zhu Q, Huynh C, Sivaramakrishnan P, Preston E, Dueck H, Stefanik D, Tan K,
1271 Trapnell C, Kim J, Waterston RH, Murray JI. 2019. A lineage-resolved molecular atlas of

1272 C. elegans embryogenesis at single-cell resolution. *Science* **365**.
1273 doi:10.1126/science.aax1971
1274 Park S-K, Gunaratne GS, Chulkov EG, Moehring F, McCusker P, Dosa PI, Chan JD, Stucky
1275 CL, Marchant JS. 2019. The anthelmintic drug praziquantel activates a schistosome
1276 transient receptor potential channel. *J Biol Chem* **294**:18873–18880.
1277 doi:10.1074/jbc.AC119.011093
1278 Peter N. Inglis, Guangshuo Ou, Michel R. Leroux, and Jonathan M. Scholey. 2006. The
1279 sensory cilia of Caenorhabditis elegans In: The C. elegans Research Community, editor.
1280 WormBook. WormBook ed. doi:doi/10.1895/wormbook.1.126.1
1281 Philogene MC, Small SGM, Wang P, Corsi AK. 2012. Distinct Caenorhabditis elegans HLH-
1282 8/twist-containing dimers function in the mesoderm. *Dev Dyn* **241**:481–492.
1283 doi:10.1002/dvdy.23734
1284 Qing X, Kulkeaw K, Wongkamchai S, Tsui SK-W. 2021. Mitochondrial Genome of Brugia
1285 malayi Microfilariae Isolated From a Clinical Sample. *Frontiers in Ecology and Evolution*
1286 **9**:25. doi:10.3389/fevo.2021.637805
1287 Rao UR, Chandrashekar R, Subrahmanyam D. 1987. Effect of ivermectin on serum dependent
1288 cellular interactions to Dipetalonema viteae microfilariae. *Trop Med Parasitol* **38**:123–127.
1289 Rathaur S, Robertson BD, Selkirk ME, Maizels RM. 1987. Secretory acetylcholinesterases
1290 from Brugia malayi adult and microfilarial parasites. *Mol Biochem Parasitol* **26**:257–265.
1291 doi:10.1016/0166-6851(87)90078-8
1292 Razin SV, Borunova VV, Maksimenko OG, Kantidze OL. 2012. Cys2His2 zinc finger protein
1293 family: classification, functions, and major members. *Biochemistry* **77**:217–226.
1294 doi:10.1134/S0006297912030017
1295 Reaves BJ, Wallis C, McCoy CJ, Lorenz WW, Rada B, Wolstenholme AJ. 2018. Recognition
1296 and killing of Brugia malayi microfilariae by human immune cells is dependent on the
1297 parasite sample and is not altered by ivermectin treatment. *Int J Parasitol Drugs Drug*

1298 *Resist* **8**:587–595. doi:10.1016/j.ijpddr.2018.09.002
1299 Ritz C, Baty F, Streibig JC, Gerhard D. 2015. Dose-Response Analysis Using R. *PLoS One*
1300 **10**:e0146021. doi:10.1371/journal.pone.0146021
1301 Roberts L, Schmidt GD, Janovy J Jr. 2009. Foundations of Parasitology. McGraw-Hill
1302 Education.
1303 Sundaram MV, Buechner M. 2016. The Caenorhabditis elegans Excretory System: A Model for
1304 Tubulogenesis, Cell Fate Specification, and Plasticity. *Genetics* **203**:35–63.
1305 doi:10.1534/genetics.116.189357
1306 Taylor SR, Santpere G, Weinreb A, Barrett A, Reilly MB, Xu C, Varol E, Oikonomou P,
1307 Glenwinkel L, McWhirter R, Poff A, Basavaraju M, Rafi I, Yemini E, Cook SJ, Abrams A,
1308 Vidal B, Cros C, Tavazoie S, Sestan N, Hammarlund M, Hobert O, Miller DM 3rd. 2021.
1309 Molecular topography of an entire nervous system. *Cell* **184**:4329–4347.e23.
1310 doi:10.1016/j.cell.2021.06.023
1311 Teufel F, Almagro Armenteros JJ, Johansen AR, Gíslason MH, Pihl SI, Tsirigos KD, Winther O,
1312 Brunak S, von Heijne G, Nielsen H. 2022. SignalP 6.0 predicts all five types of signal
1313 peptides using protein language models. *Nat Biotechnol* **40**:1023–1025.
1314 doi:10.1038/s41587-021-01156-3
1315 Tongu Y. 1974. Ultrastructural studies on the microfilaria of Brugia malayi. *Acta Med Okayama*
1316 **28**:219–242.
1317 Ton TGN, Mackenzie C, Molyneux DH. 2015. The burden of mental health in lymphatic
1318 filariasis. *Infect Dis Poverty* **4**:34. doi:10.1186/s40249-015-0068-7
1319 U. R. Rao, A. C. Vickery, B. H. Kwa, J. K. Nayar. 1992. Brugia Malayi: Ivermectin Inhibits the
1320 Exsheathment of Microfilariae. *ASTMH* **46**:183–188. doi:10.4269/ajtmh.1992.46.183
1321 Vatta AF, Dzimianski M, Storey BE, Camus MS, Moorhead AR, Kaplan RM, Wolstenholme AJ.
1322 2014. Ivermectin-dependent attachment of neutrophils and peripheral blood mononuclear
1323 cells to Dirofilaria immitis microfilariae in vitro. *Vet Parasitol* **206**:38–42.

1324 doi:10.1016/j.vetpar.2014.02.004
1325 Verma S, Kashyap SS, Robertson AP, Martin RJ. 2020. Diethylcarbamazine activates TRP
1326 channels including TRP-2 in filaria, Brugia malayi. *Communications Biology* **3**:398.
1327 doi:10.1038/s42003-020-01128-4
1328 Weiss MG. 2008. Stigma and the social burden of neglected tropical diseases. *PLoS Negl Trop*
1329 *Dis* **2**:e237. doi:10.1371/journal.pntd.0000237
1330 Williams PDE, Kashyap SS, McHugh MA, Robertson AP, Martin RJ. 2022.
1331 Diethylcarbamazine, TRP channels and Ca2+ signaling in cells of the Ascaris intestine.
1332 *Research Square*. doi:10.21203/rs.3.rs-1262219/v1
1333 Wolf FA, Angerer P, Theis FJ. 2018. SCANPY: large-scale single-cell gene expression data
1334 analysis. *Genome Biol* **19**:15. doi:10.1186/s13059-017-1382-0
1335 Wolstenholme AJ, Evans CC, Jimenez PD, Moorhead AR. 2015. The emergence of
1336 macrocyclic lactone resistance in the canine heartworm, Dirofilaria immitis. *Parasitology*
1337 **142**:1249–1259. doi:10.1017/S003118201500061X
1338 World Health Organization. 2018. Guideline: Alternative Mass Drug Administration Regimens
1339 to Eliminate Lymphatic Filariasis. Geneva: World Health Organization.
1340 Wu Y, Preston G, Bianco AE. 2008. Chitinase is stored and secreted from the inner body of
1341 microfilariae and has a role in exsheathment in the parasitic nematode Brugia malayi. *Mol*
1342 *Biochem Parasitol* **161**:55–62. doi:10.1016/j.molbiopara.2008.06.007
1343 Xu S, Liu C, Tzertzinis G, Ghedin E, Evans CC, Kaplan R, Unnasch TR. 2011. In vivo
1344 transfection of developmentally competent Brugia malayi infective larvae. *Int J Parasitol*
1345 **41**:355–362. doi:10.1016/j.ijpara.2010.10.005
1346 Young MD, Behjati S. 2020. SoupX removes ambient RNA contamination from droplet-based
1347 single-cell RNA sequencing data. *Gigascience* **9**. doi:10.1093/gigascience/giaa151
1348 Zahner H, Schmidtchen D, Mutasa JA. 1997. Ivermectin-induced killing of microfilariae in vitro
1349 by neutrophils mediated by NO. *Exp Parasitol* **86**:110–117. doi:10.1006/expr.1997.4160

1350 Zamanian M, Fraser LM, Agbedanu PN, Harischandra H, Moorhead AR, Day TA, Bartholomay
1351 LC, Kimber MJ. 2015. Release of Small RNA-containing Exosome-like Vesicles from the
1352 Human Filarial Parasite Brugia malayi. *PLoS Negl Trop Dis* **9**:e0004069.
1353 doi:10.1371/journal.pntd.0004069
1354 Zhang S, Banerjee D, Kuhn JR. 2011. Isolation and culture of larval cells from C. elegans.
1355 *PLoS One* **6**:e19505. doi:10.1371/journal.pone.0019505

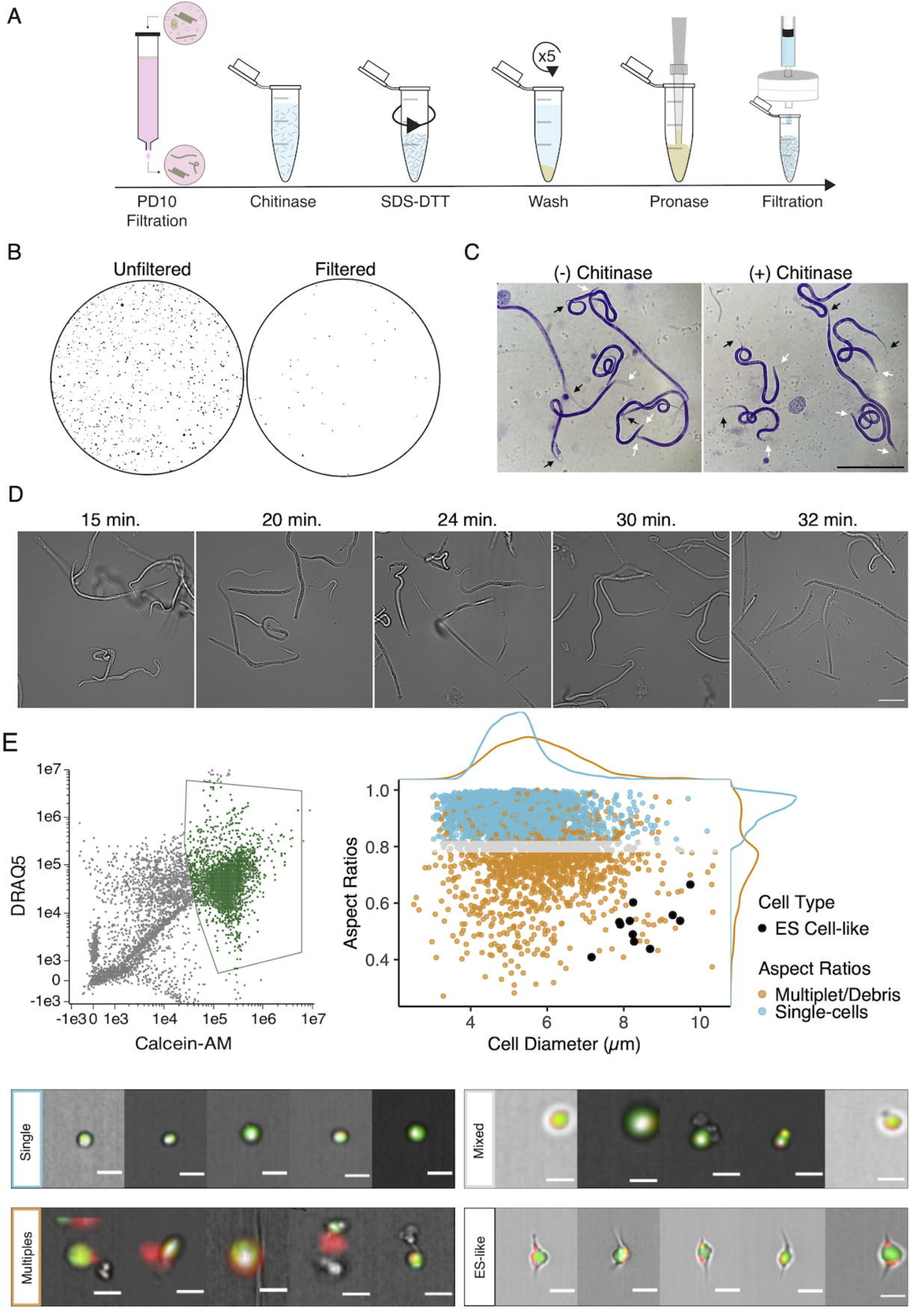
A
x5
PD10 Filtration
Chitinase
SDS-DTT
Wash
Pronase
Filtration
B
Unfiltered
Filtered
C
(-) Chitinase
(+) Chitinase
D
15 min.
20 min.
24 min.
30 min.
32 min.
E
DRAQ5
Calcein-AM
1e7
1e6
1e5
1e4
1e3
0
-1e3
-1e3 0 1e3 1e4 1e5 1e6 1e7
Aspect Ratios
1.0
0.8
0.6
0.4
4 6 8 10
Cell Diameter (μm)
Cell Type
ES Cell-like
Aspect Ratios
Multiplet/Debris
Single-cells
Single
Mixed
Multiples
ES-like

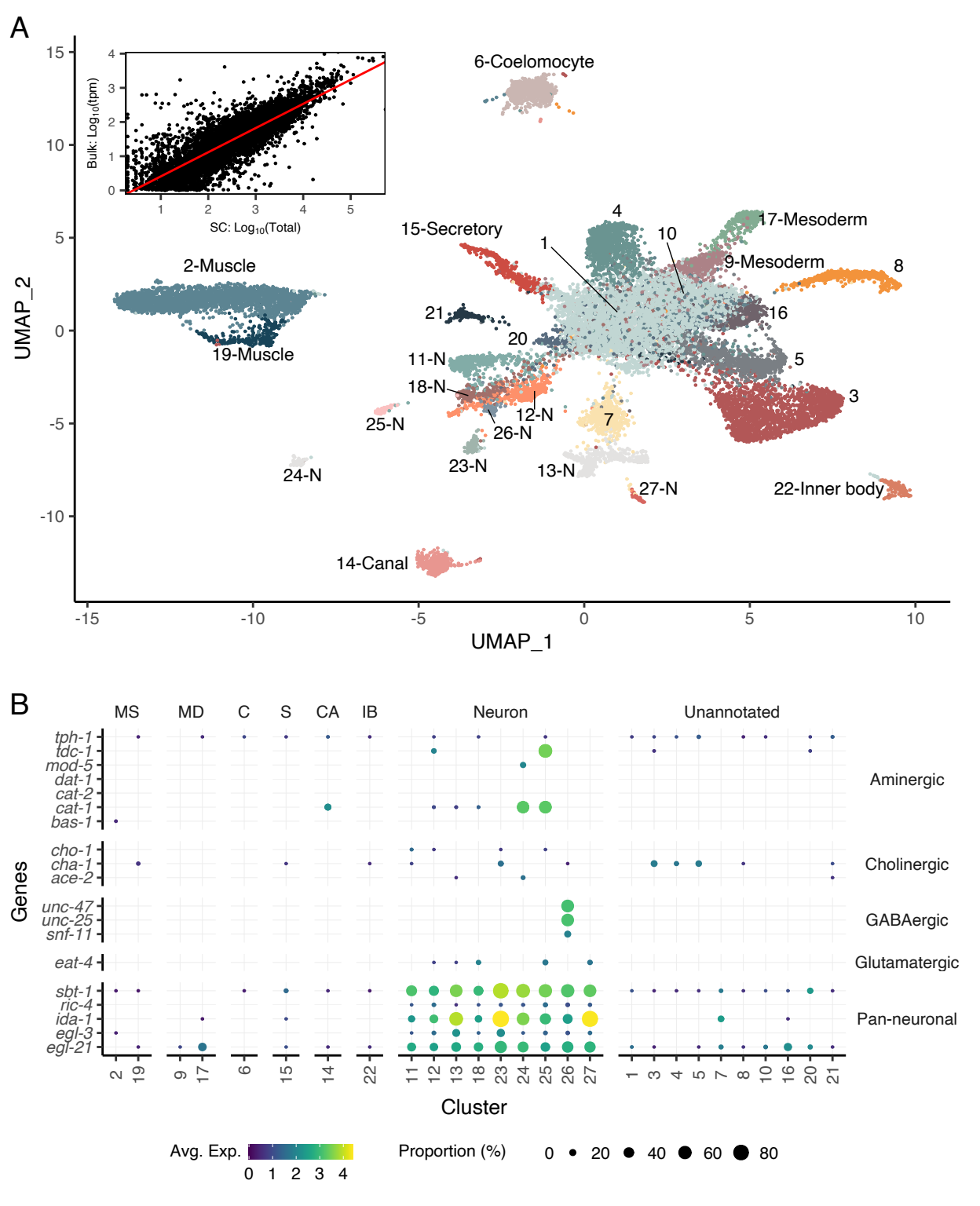
A
Bulk: Log10(tpm)
SC: Log10(Total)
6-Coelomocyte
15-Secretory
17-Mesoderm
9-Mesoderm
2-Muscle
19-Muscle
11-N
18-N
12-N
26-N
25-N
23-N
24-N
13-N
27-N
22-Inner body
14-Canal
UMAP_2
UMAP_1
B
MS
MD
C
S
CA
IB
Neuron
Unannotated
tph-1
tdc-1
mod-5
dat-1
cat-2
cat-1
bas-1
Aminergic
cho-1
cha-1
ace-2
Cholinergic
unc-47
unc-25
snf-11
GABAergic
eat-4
Glutamatergic
sbt-1
ric-4
ida-1
egl-3
egl-21
Pan-neuronal
Genes
Cluster
Avg. Exp.
Proportion (%)

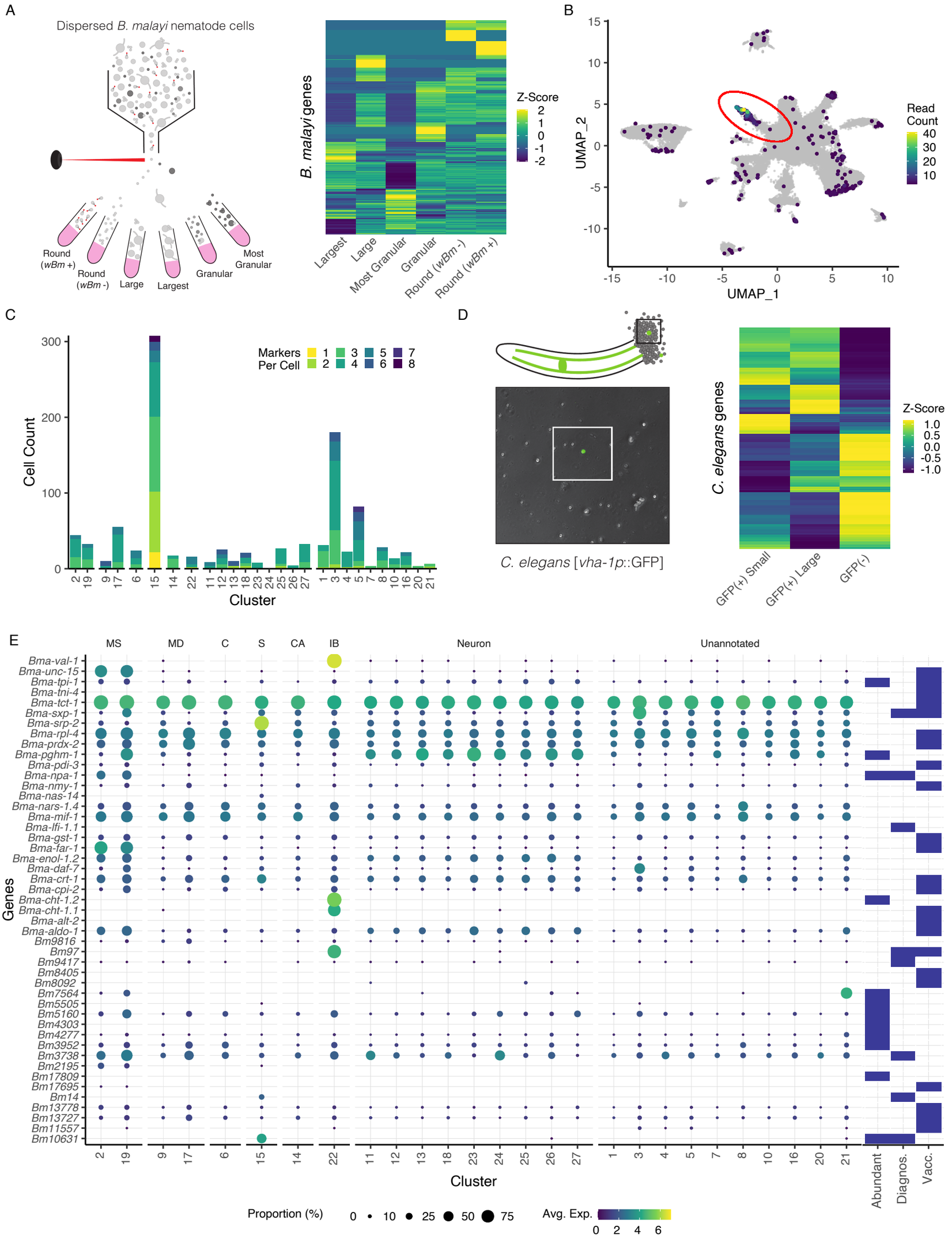
A
Dispersed B. malayi nematode cells
Round (wBm +)
Round (wBm -)
Large
Largest
Granular
Most Granular
B. malayi genes
Z-Score
2
1
0
-1
-2
Largest
Large
Most Granular
Granular
Round (wBm -)
Round (wBm +)
B
UMAP_2
UMAP_1
Read Count
40
30
20
10
C
Cell Count
Markers Per Cell
1 2 3 4 5 6 7 8
Cluster
D
C. elegans [vha-1p::GFP]
C. elegans genes
Z-Score
1.0
0.5
0.0
-0.5
-1.0
GFP(+) Small
GFP(+) Large
GFP(-)
E
MS
MD
C
S
CA
IB
Neuron
Unannotated
Genes
Cluster
Abundant
Diagnos.
Vacc.
Proportion (%)
0 10 25 50 75
Avg. Exp.
0 2 4 6

A
S
n=79
MS
n=384
MD
n=254
C
n=176
CA
n=53
IB
n=70
N
n=498
Signal Peptide
No
Yes
B
TM Domains
0
1
2
3
4
5
6
7
8
9
10
11
12
13
15
16
19
23
C
Proportion (%)
5
10
25
50
75
Avg. Exp.
0
1
2
3
Unannotated
Neuron
IB
CA
S
C
MD
MS
Cluster
C2H2 ZF TFs

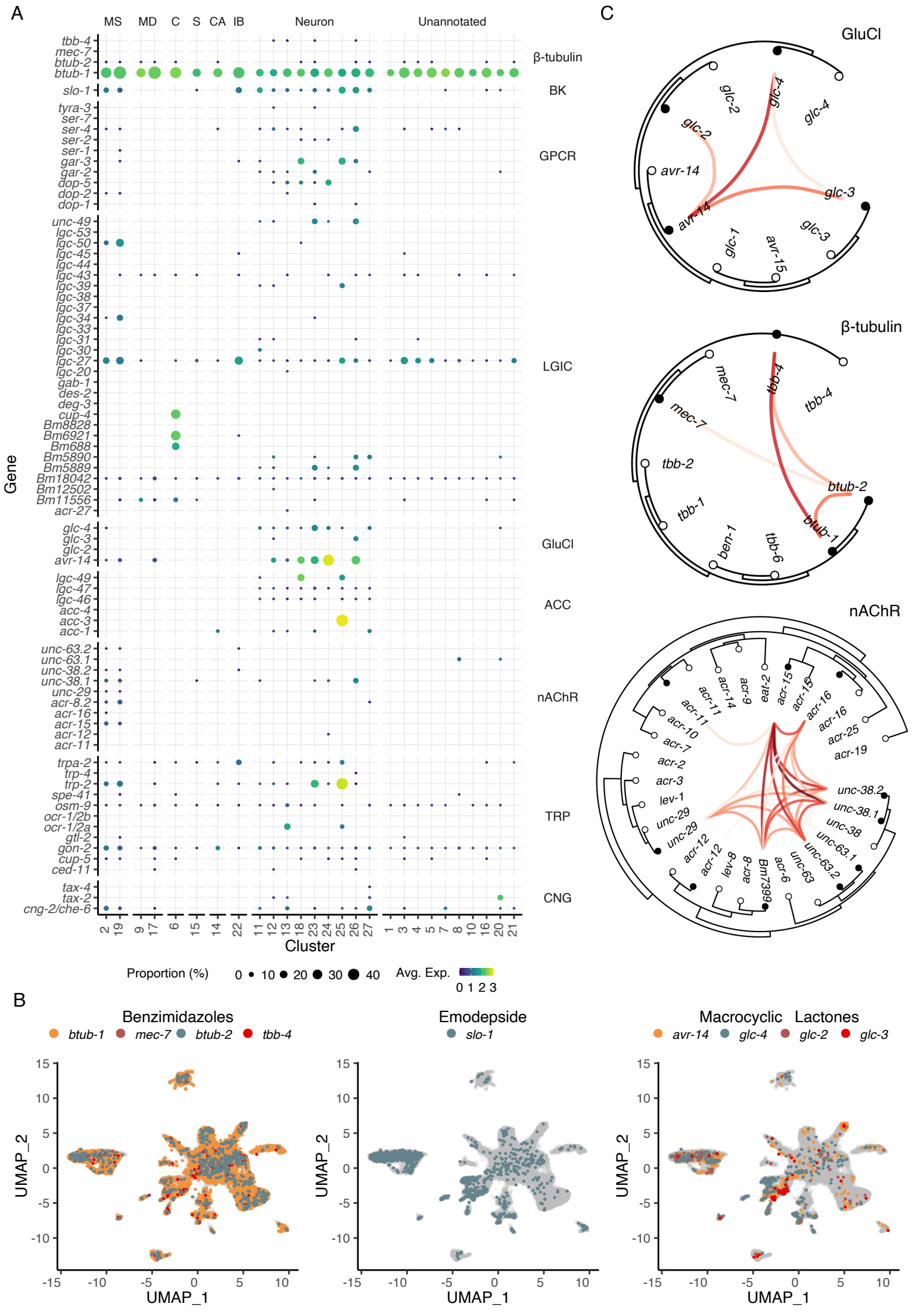
A
MS
MD
C
S
CA
IB
Neuron
Unannotated
β-tubulin
BK
GPCR
LGIC
GluCl
ACC
nAChR
TRP
CNG
Gene
Cluster
Proportion (%)
0 10 20 30 40
Avg. Exp.
0 1 2 3
C
GluCl
β-tubulin
nAChR
B
Benzimidazoles
btub-1 mec-7 btub-2 tbb-4
Emodepside
slo-1
Macrocyclic Lactones
avr-14 glc-4 glc-2 glc-3
UMAP_1
UMAP_2

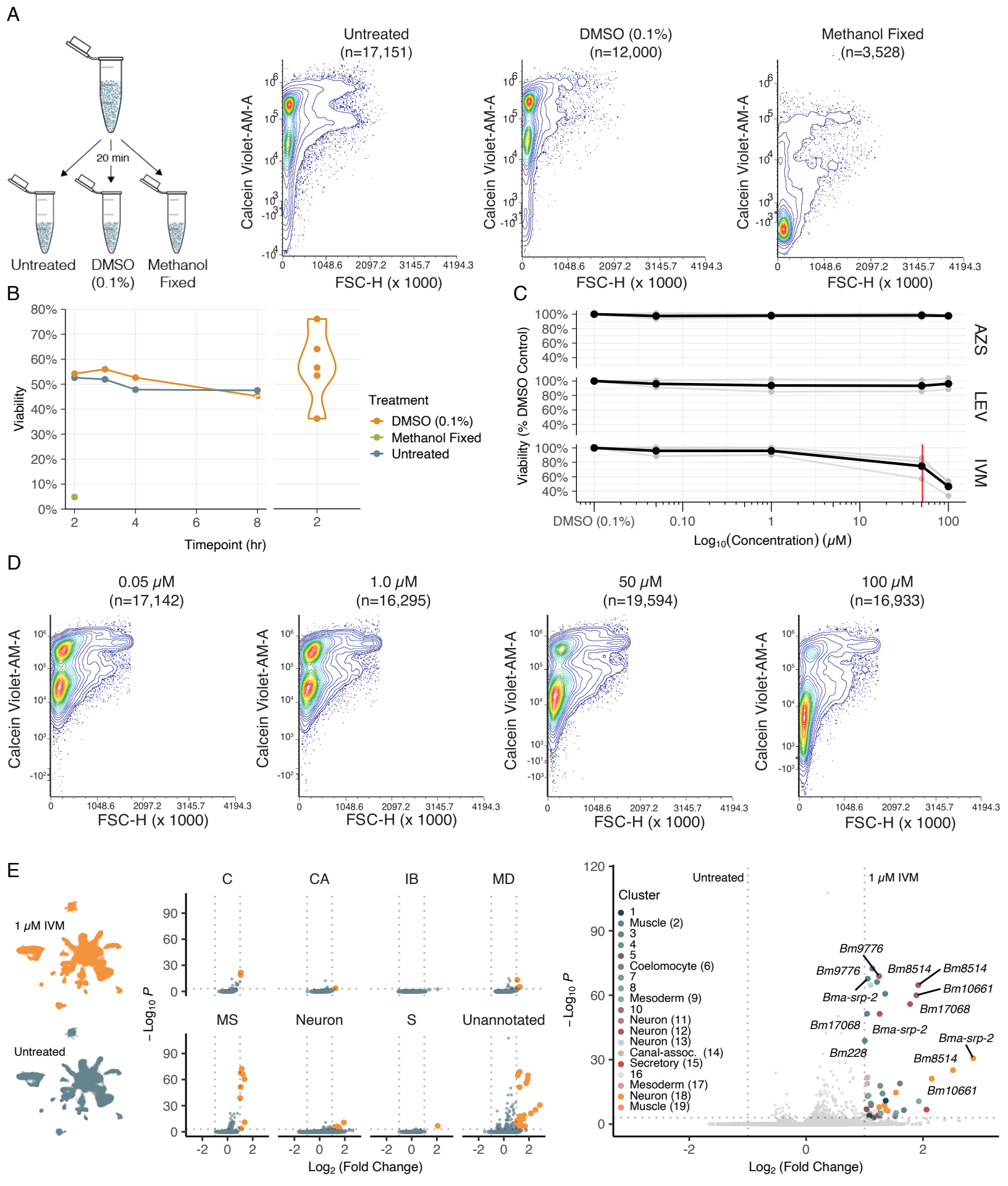
A
20 min
Untreated
DMSO (0.1%)
Methanol Fixed
Untreated (n=17,151)
DMSO (0.1%) (n=12,000)
Methanol Fixed (n=3,528)
Calcein Violet-AM-A
FSC-H (x 1000)
B
Viability
Timepoint (hr)
Treatment
DMSO (0.1%)
Methanol Fixed
Untreated
C
Viability (% DMSO Control)
AZS
LEV
IVM
DMSO (0.1%)
Log10(Concentration) (μM)
D
0.05 μM (n=17,142)
1.0 μM (n=16,295)
50 μM (n=19,594)
100 μM (n=16,933)
E
1 μM IVM
Untreated
C
CA
IB
MD
MS
Neuron
S
Unannotated
−Log10 P
Log2 (Fold Change)
Cluster
1
Muscle (2)
3
4
5
Coelomocyte (6)
7
8
Mesoderm (9)
10
Neuron (11)
Neuron (12)
Neuron (13)
Canal-assoc. (14)
Secretory (15)
16
Mesoderm (17)
Neuron (18)
Muscle (19)
Bm9776
Bm8514
Bm10661
Bma-srp-2
Bm17068
Bm228

A

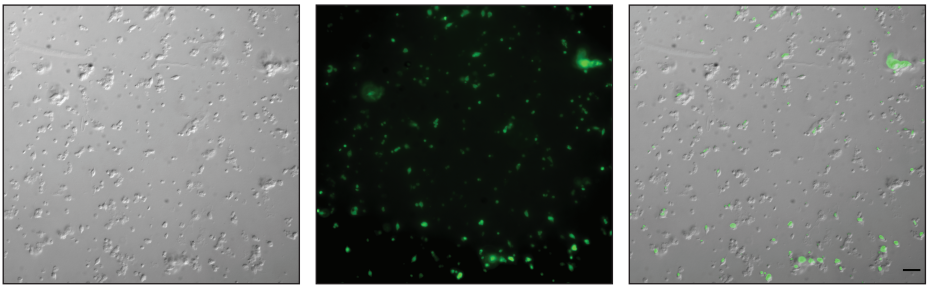
Brightfield
Calcein-AM
Composite

B

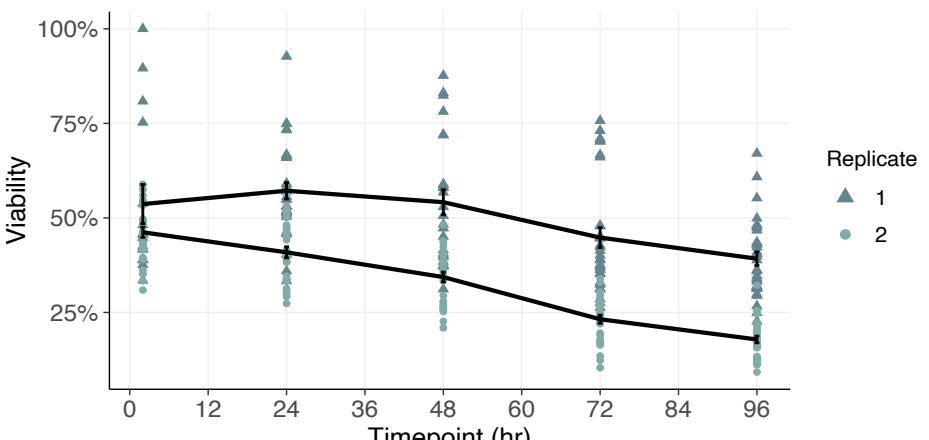
100%
75%
50%
25%
Viability
0
12
24
36
48
60
72
84
96
Timepoint (hr)
Replicate
1
2